AIMS Mathematics, 9(10): 27627–27663.
DOI: 10.3934/math.20241342
Received: 24 July 2024
Revised: 03 September 2024
Accepted: 13 September 2024
Published: 24 September 2024

https://www.aimspress.com/journal/Math

Research article

Time-delayed control of a nonlinear self-excited structure driven by simultaneous primary and 1:1 internal resonance: analytical and numerical investigation

Nasser. A. Saeed[1,2,3,4,5,*], Amal Ashour[6], Lei Hou[4], Jan Awrejcewicz[5] and Faisal Z. Duraihem[7]

[1] Department of Physics and Engineering Mathematics, Faculty of Electronic Engineering, Menouf 32952, Menoufia University, Egypt
[2] Mathematics Department, Faculty of Science, Galala University, Galala City 43511, Egypt
[3] Applied Science Research Center. Applied Science Private University, Amman, Jordan
[4] School of Astronautics, Harbin Institute of Technology, Harbin 150001, China
[5] Department of Automation, Biomechanics, and Mechatronics, Faculty of Mechanical Engineering, Lodz University of Technology, 90924 Lodz, Poland
[6] Department of Basic Science, Menoufia Higher Institute of Engineering and Technology, El-Bagour 32821, Egypt
[7] Department of Mathematics, College of Science, King Saud University, P.O. Box 2455, Riyadh 11451, Saudi Arabia

* **Correspondence:** Email: Nasser.A.Saeed@el-eng.menofia.edu.eg.

Abstract: Main objective of this research to eliminate the resonant vibrations and stabilize the unstable motion of a self-excited structure through the implementation of an innovative active control strategy. The control strategy coupling the self-excited structure with a second-order filter, which feedback gain λ and control gain β, as well as a first-order filter, which feedback gain δ and control gain γ. The coupling of the second-order filter to establish an energy bridge between the structure and the filter to pump out the structure's vibration energy to the filter. In contrast, the primary purpose of coupling the first-order filter to stabilize the closed loop by adjusting the damping of the system using the control keys δ and γ. Accordingly, the mathematical model of the proposed control system formulated, incorporating the closed-loop time delay τ. An analytical solution for the system model obtained, and a nonlinear algebraic system for the steady-state dynamics of the controlled structure extracted. The system's bifurcation characteristics analyzed in the form of stability charts and response curves. Additionally, the system's full response simulated numerically. Findings the high performance of the introduced controller in eliminating the structure's resonant vibrations and stabilizing non-resonant unstable motion. In addition, analytical and numerical investigations revealed that the frequency band

within which the second-order filter can absorb the structure's resonant oscillation relies on the algebraic product of β and λ. Furthermore, it was found that the equivalent damping of the system depends on the algebraic product of γ and δ, which can be employed to stabilize the negatively damped self-excited systems. Finally, it reported that although the loop delay can potentially degrade vibration control performance, the time-delay stability margin is nonlinearly proportional to the product of γ and δ. This finding that increasing the value of $\gamma \times \delta$ can compensate for the adverse effects of loop delay on both system stability and vibration suppression efficiency.

Keywords: vibration control; time delay control system; resonance; self-excited structure; Poincaré section and bifurcation diagram; stability margin; 0-1 chaotic test
Mathematics Subject Classification: 34A34, 34C15, 34C23, 34C25, 34D20, 34E13, 37N15, 70B05, 70K05, 70K40, 70K42, 70K50

1. Introduction

Self-excited oscillations, also called flutter or self-sustained oscillations, are a notable and prevalent occurrence in a wide range of different engineering structures and systems. These oscillations arise due to the interactions among restoring and inertial forces within the systems, which occur even when the driving forces are negligible [1]. Self-excited oscillations may cause undesired effects on the engineering system, such as performance degradation, structural instability, and catastrophic destruction. The collapse of the Tacoma Bridge in 1940 due to wind-induced oscillations is a notable example of the dangers of self-excited structures [2]. Understanding the mechanisms of inducing this type of vibration as well as providing the control strategies to overcome their negative effect are crucial in engineering systems and structural design. Self-excitation primarily arises from a distinct type of driving force, which uniquely amplifies the driving force at low velocities and reduces the driving force at high velocities within the targeted structure [3]. In real-world scenarios, self-excited vibrations can arise when fluid or wind consistently flows over-engineering structures, such as aircraft wings, causing structural vibrations. The mathematical interpretation for the occurrence of these self-excitations is the presence of nonlinear damping in the governing equations of motion for such structures, which often initiates these destructive oscillations. Two commonly used models to represent nonlinear damping-induced self-excitations are Rayleigh damping, expressed mathematically as $f_R = (-\mu_R\dot{y} + \gamma_R\dot{y}^3)$ and Van-der-Pol damping, defined by the mathematical model $f_V = (-\mu_V\dot{y} + \gamma y^2\dot{y})$. Although f_R and f_V seem to be mathematically different, Warminski [4] has shown that these two models are essentially equivalent.

The literature presents a variety of control strategies designed to enhance dynamic characteristics and eliminate resonant vibrations in engineering systems. Among these, state feedback control is a key technique. For example, cubic velocity controllers are frequently used to mitigate primary resonance vibrations caused by both parametric [5] and external excitations [6,7]. Linear position-velocity control is another method, effective in suppressing primary and secondary resonances in externally excited single-degree-of-freedom systems [8–11]. Position feedback primarily alters the natural frequencies of the system to avoid resonance, while velocity feedback adjusts damping to reduce oscillatory behavior. In [12], linear position-velocity control effectively suppresses nonlinear oscillations in a 2-DOF system subjected to both external and multiparametric excitations. Moreover, acceleration feedback control has shown superior efficiency compared to position and velocity control in managing principal parametric excitations [13]. A recently developed technique, the Integral Resonant Controller (IRC),

couples the targeted oscillatory system with a first-order differential equation (linear or nonlinear) using feedback and control parameters [14–16]. IRC effectively minimizes undesirable vibrations in a range of engineering systems across various excitation and resonance conditions [17–20]. Melcean and Sumeet [17] analytically and numerically evaluated IRC for controlling transverse vibrations in micro-sized cantilever beams driven by primary harmonic excitation. Saeed et al. [18] explored vibration suppression in a parametrically driven one-DOF nonlinear system using a time-delayed IRC. Furthermore, Saeed et al. [19,20] used a combination of two IRCs to control resonant vibrations in a 2-DOF system, simulating lateral oscillations in an active magnetic bearing rotor. Additionally, well-established control strategies such as positive position feedback (PPF) control and nonlinear saturation control (NSC) are prevalent in the literature. PPF control works by coupling the targeted oscillatory system to a second-order differential equation through linear feedback and control parameters, creating an energy bridge to transfer oscillatory energy from the system to the controller [21,22]. Tuning the PPF natural frequency to match the target system's driving frequency optimizes energy transfer to the controller [23,24]. Saeed et al. [25] explored an adaptive PPF controller through numerical and analytical studies, while Dhobale and Chatterjee [26] demonstrated excellent performance in eliminating resonance vibration with an experimental adaptive PPF control. NSC, one of the oldest vibration mitigation mechanisms, was identified by Nayfeh et al. [27] in studies on ships' pitch-roll interactions. This control strategy involves coupling the targeted system to a second-order system nonlinearity to achieve 2:1 internal resonance, effectively transferring energy from the primary system to the absorber [28,29].

In the realm of vibration control for self-excited structures, numerous strategies have been employed to mitigate flutter phenomena and stabilize unstable oscillations. These efforts encompass all the control strategies, each aimed at enhancing system stability and performance. El-Badawy and Nasr El-Deen [30] were the pioneers in NSC to regulate self-excited oscillators, targeting nonlinear vibrations in a Rayleigh-type unforced system. They observed some oscillation reduction but did not emphasize controller robustness. Jun et al. [31] examined NSC for self-excited vibrations without external excitation, finding limited mitigation effects. Warminski et al. [32] used NSC on a forced self-excited oscillator, discovering that it destabilized the system at resonance with low damping. Even though they reported that increasing the damping improved stability but reduced the controller's effectiveness. The arising of time delay in active control systems is an unavoidable phenomenon [33–36], primarily due to the analog-to-digital conversion and its reverse process. Sarker et al. [37] studied time-delayed PPF control for the same self-excited structure in [32], noting that time delay negatively impacted performance. They found that increasing loop gain could counteract this issue. They incorporated a predetermined time delay and re-optimized the system to achieve stable static equilibrium. Saeed et al. [38] used time-delayed IRC to stabilize nonlinear oscillations and eliminate resonant vibrations in the same structure studied in [32,37]. Their analysis indicated that IRC could stabilize unstable motions and mitigate resonance vibrations, although it could not eliminate vibrations entirely. Mondal et al. [39,40] investigated velocity and acceleration feedback control for unwanted vibrations in a Rayleigh-type self-excited structure. They found that optimal filter parameters could effectively reduce or suppress vibrations, but time delays in the closed-loop system adversely affected performance. To address this, they suggested increasing the loop gain to improve overall performance.

Within this work, a comprehensive study of a novel control method aimed at eliminating strong oscillations in self-excited structures at resonant conditions as well as stabilizing the system's low oscillations away from the resonance is presented. The proposed control strategy involves coupling the self-excited structure with two filters, one of a second-order filter and the other of a first-order filter. The second-order filter's primary task is to establish an energy bridge with the structure at the

resonant frequency band to channel the strong resonant oscillation from the structure to the filter. The first-order filter's main goal is to adjust the negative linear damping of the structure to stabilize the unstable non-resonant oscillations and enhance the performance of the second-order filter. Given that the proposed strategies involve a closed-loop control system, including digital processing for the measured and applied control signals, the effect of loop delay on system stability has been included in this study. A detailed investigation of each control parameter's effect, as well as the loop delay on control performance, has been conducted.

2. Time-delayed control system

The nonlinear mathematical model that describes the transverse vibrations of a self-excited beam system subjected to large deflections, considering only the first bending mode, as shown in Figure 1(a), is expressed as follows [41]:

$$\ddot{x}_1 - \mu_1\dot{x}_1 + \omega_1^2 x_1 + \alpha_1 x_1^3 + \alpha_2\dot{x}_1^3 + \alpha_3\left(x_1\dot{x}_1^2 + x_1^2\ddot{x}_1\right) = \Omega^2 f\cos\left(\Omega t\right) + W, \tag{1}$$

where $x_1(t)$, $\dot{x}_1(t)$, $\ddot{x}_1(t)$ represent the displacement, velocity, and acceleration of the structure, f denotes the driving force amplitude, Ω is the driving frequency, and W denotes the proposed control signal. Building on the various control methodologies presented in the literature [30–32,37–40], this work introduces a novel control technique. The control strategy involves coupling the self-excited structure given by Eq (1) with a second-order filter, which incorporates feedback gain λ and control gain β, as well as a first-order filter, which utilizes feedback gain δ and control gain γ resulting in the following closed-loop system:

$$\ddot{x}_1 - \mu_1\dot{x}_1 + \omega_1^2 x_1 + \alpha_1 x_1^3 + \alpha_2\dot{x}_1^3 + \alpha_3\left(x_1\dot{x}_1^2 + x_1^2\ddot{x}_1\right) = \Omega^2 f\cos\left(\Omega t\right) + \beta x_2(t-\tau) + \gamma x_3(t-\tau), \tag{2}$$

$$\ddot{x}_2 + \mu_2\dot{x}_2 + \omega_2^2 x_2 = \lambda x_1(t-\tau), \tag{3}$$

$$\dot{x}_3 + \rho x_3 = \delta x_1(t-\tau), \tag{4}$$

where $x_2(t)$, $\dot{x}_2(t)$, $\ddot{x}_2(t)$ are the displacement, velocity, and acceleration of the controller. Additionally, $x_3(t)$ and $\dot{x}_3(t)$ represent the displacement and velocity of the first-order filter used as a vibration damper in the closed-loop control system, while the proposed control signal $W = \beta x_2(t-\tau) + \gamma x_3(t-\tau)$. The physical interconnection between the structure and the controller is illustrated in Figure 1(a). Additionally, the block diagram in Figure 1(b) demonstrates the sequential execution of the proposed control system. In this setup, a Micro-Fiber Composite (MFC) sensor measures transversal displacement $x_1(t)$ of the beam system, which is then input into a digital controller (i.e., computer). Within the computer, $x_1(t)$ is amplified using two different feedback gains, δ and λ. The manipulated signals may encounter a time delay τ due to analog-to-digital conversions. Following this, the manipulated signals, $\lambda x_1(t-\tau)$ and $\delta x_1(t-\tau)$, are used to excite second-order and first-order filters, respectively. The states of these excited filters (i.e., $x_2(t)$ and $x_3(t)$) are then amplified by gains β and γ and subjected to a loop delay τ to formulate the control signal $W = \beta x_2(t-\tau) + \gamma x_3(t-\tau)$. Finally, the generated control signal is applied to the periodically excited structure via an MFC actuator to suppress the unwanted vibrations of the system.

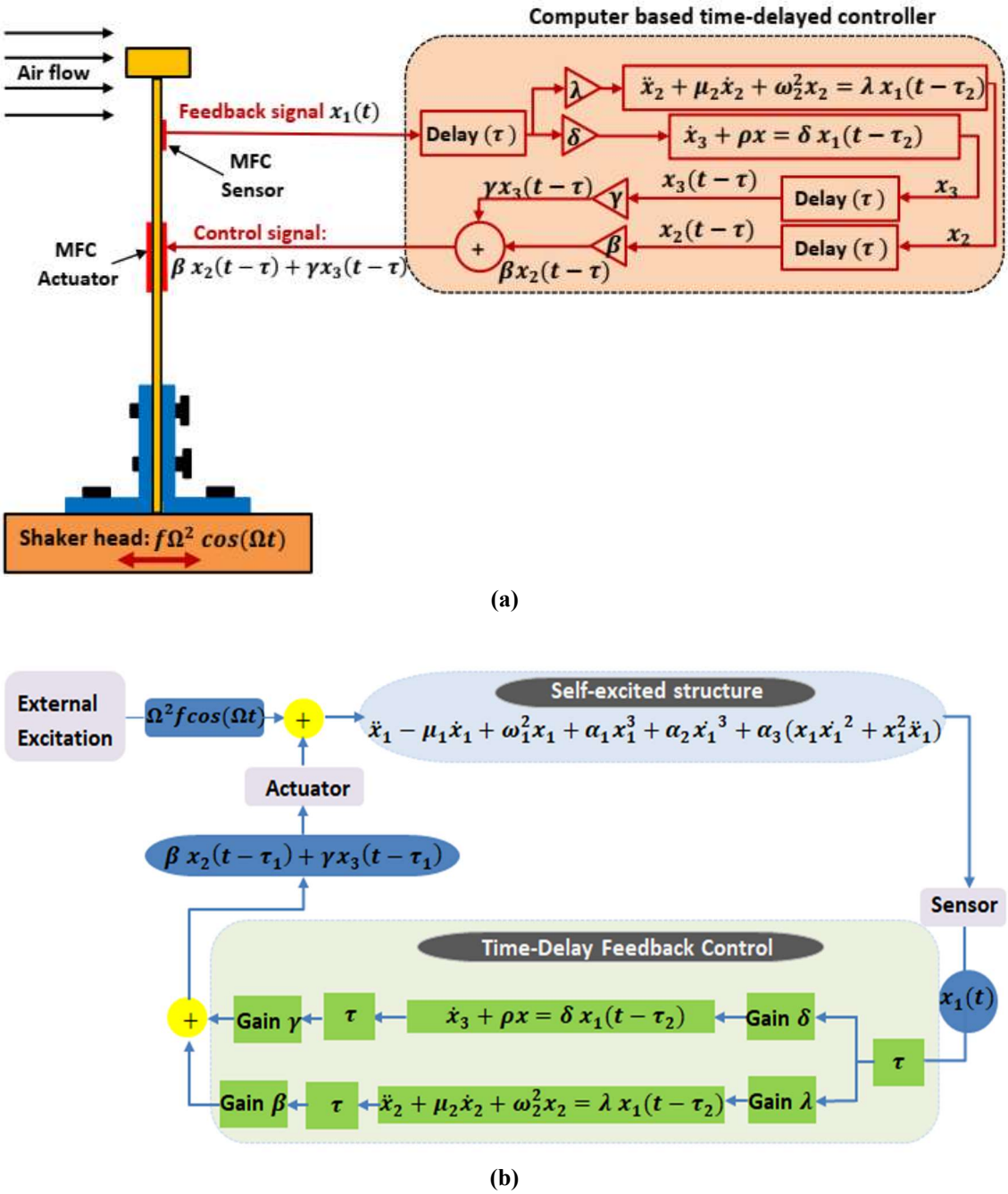

Figure 1. Time-delayed control of self-excited structure: (a) Physical connection between the self-excited beam system and the proposed controller, and (b) Signal flow chart between the system and controller.

3. Nonlinear analysis, stability, and steady-state solution

To evaluate the efficiency of the considered time-delayed control system, an analytical investigation of the coupled nonlinear system described by Eqs (2)–(4) is conducted using the multiple scales technique [42]. Accordingly, the approximate solution of Eqs (2)–(4) can be assumed as follows:

$$x_1(t,\varepsilon) = x_{10}(t_0,t_1) + \varepsilon x_{11}(t_0,t_1), \tag{5}$$

$$x_2(t,\varepsilon) = x_{20}(t_0,t_1) + \varepsilon x_{21}(t_0,t_1), \tag{6}$$

$$x_3(t,\varepsilon) = \varepsilon x_{30}(t_0,t_1) + \varepsilon^2 x_{31}(t_0,t_1) \tag{7}$$

where $t_0 = t$ and $t_1 = \varepsilon t$ are the time scales. Therefore, in terms of t_0 and t_1 the derivatives d/dt and d^2/dt^2 can be expressed as follows:

$$d/dt = D_0 + \varepsilon D_1,\ d^2/dt^2 = D_0^2 + 2\varepsilon D_0 D_1,\ D_j = \partial/\partial t_j \quad j = 0, 1\ . \tag{8}$$

Additionally, the delayed states $x_1(t-\tau),\ x_2(t-\tau),$ and $x_3(t-\tau)$ can be expressed based on Eqs (5)–(7) as follows:

$$x_1(t-\tau,\varepsilon) = x_{10\tau}(t_0,t_1) + \varepsilon x_{11\tau}(t_0,t_1), \tag{9}$$

$$x_2(t-\tau,\varepsilon) = x_{20\tau}(t_0,t_1) + \varepsilon x_{21\tau}(t_0,t_1), \tag{10}$$

$$x_3(t-\tau,\varepsilon) = \varepsilon x_{30\tau}(t_0,t_1) + \varepsilon^2 x_{31\tau}(t_0,t_1). \tag{11}$$

To apply perturbation analysis, the system parameters should be rescaled as follows:

$$\begin{aligned}&\mu_1 = \varepsilon\tilde{\mu}_1,\ \mu_2 = \varepsilon\tilde{\mu}_2, \alpha_1 = \varepsilon\tilde{\alpha}_1, \alpha_2 = \varepsilon\tilde{\alpha}_2, \alpha_3 = \varepsilon\tilde{\alpha}_3,\ \eta = \varepsilon\tilde{\eta},\ \beta_1 = \varepsilon\tilde{\beta}_1,\ \beta_2 = \varepsilon\tilde{\beta}_2, \lambda = \varepsilon\tilde{\lambda},\\ &\delta = \varepsilon\tilde{\delta},\ f = \varepsilon\tilde{f}.\end{aligned} \tag{12}$$

Substituting Eqs (5)–(12) into Eqs (2)–(4), we can obtain the following linear time-delayed differential equations:

O (ε^0):

$$(D_0^2 + \omega_1^2)x_{10} = 0, \tag{13}$$

$$(D_0^2 + \omega_2^2)x_{20} = 0. \tag{14}$$

O (ε^1):

$$\begin{aligned}\left(D_0^2 + \omega_1^2\right)x_{11} = &-2D_0D_1x_{10} + \tilde{\mu}_1 D_0 x_{10} - \tilde{\alpha}_1 x_{10}^3 - \tilde{\alpha}_2 (D_0 x_{10})^3 - \tilde{\alpha}_3 (x_{10}(D_0 x_{10})^2 + x_{10}^2 D_0^2 x_{10})\\ &+ \frac{\Omega^2 \tilde{f}}{2}(e^{i\Omega t} + e^{-i\Omega t}) + \tilde{\beta} x_{20\tau} + \tilde{\gamma} x_{30\tau},\end{aligned} \tag{15}$$

$$\left(D_0^2 + \omega_2^2\right)x_{21} = -2D_0D_1x_{20} - \tilde{\mu}_2 D_0 x_{20} + \tilde{\lambda} x_{10\tau}, \tag{16}$$

$$(D_0 + \rho)x_{30} = \tilde{\delta}x_{10\tau}. \tag{17}$$

Accordingly, the solution of Eqs (13), (14), and (17) can be written such that:

$$x_{10}(t_0, t_1) = A_1(t_1)e^{i\omega_1 t_0} + \bar{A}_1(t_1)e^{-i\omega_1 t_0}, \tag{18}$$

$$x_{20}(t_0, t_1) = A_2(t_1)e^{i\omega_2 t_0} + \bar{A}_2(t_1)e^{-i\omega_2 t_0}, \tag{19}$$

$$x_{30}(t_0, t_1) = \psi A_1(t_1)e^{i\omega_1 t_0} + \bar{\psi}\bar{A}_1(t_1)e^{-i\omega_1 t_0}. \tag{20}$$

where $i = \sqrt{-1}$, $A_1(t_1)$ and $A_2(t_1)$ are unspecified functions of t_1, they will be established in the subsequent approximation step, $\bar{A}_1(t_1)$ and $\bar{A}_2(t_1)$ are the complex conjugate of $A_1(t_1)$ and $A_2(t_1)$, $\psi = \tilde{\delta}(\rho - i\omega_1)/(\rho^2 + \omega_1^2)$, and $\bar{\psi} = \tilde{\delta}(\rho + i\omega_1)/(\rho^2 + \omega_1^2)$. According to Eqs (18) and (19), the delayed functions $x_{10\tau}(t_0, t_1)$, $x_{20\tau}(t_0, t_1)$, and $x_{30\tau}(t_0, t_1)$ can be expressed as follows:

$$x_{10\tau}(t_0, t_1) = A_1(t_1 - \varepsilon\tau)e^{i\omega_1(t_0-\tau)} + \bar{A}_1(t_1 - \varepsilon\tau)e^{-i\omega_1(t_0-\tau)}, \tag{21}$$

$$x_{20\tau}(t_0, t_1) = A_2(t_1 - \varepsilon\tau)e^{i\omega_2(t_0-\tau)} + \bar{A}_2(t_1 - \varepsilon\tau)e^{-i\omega_2(t_0-\tau)}, \tag{22}$$

$$x_{30\tau}(t_0, t_1) = \psi A_1(t_1 - \varepsilon\tau)e^{i\omega_1(t_0-\tau)} + \bar{\psi}\bar{A}_1(t_1 - \varepsilon\tau)e^{-i\omega_1(t_0-\tau)}. \tag{23}$$

Expanding $A_1(t_1 - \varepsilon\tau)$ and $A_2(t_1 - \varepsilon\tau)$ in the Maclaurin series up to the first-order for the small-time delay values, we have

$$A_1(t_1 - \varepsilon\tau) \cong A_1(t_1) - \varepsilon\tau A_1'(t_1) = A_1(t_1) - \varepsilon\tau D_1 A_1(t_1), \tag{24}$$

$$A_2(t_1 - \varepsilon\tau) \cong A_2(t_1) - \varepsilon\tau A_2'(t_1) = A_2(t_1) - \varepsilon\tau D_1 A_2(t_1). \tag{25}$$

Inserting Eqs (24) and (25) into (21)–(23), we have

$$x_{10\tau}(t_0, t_1) = \left(A_1(t_1) - \varepsilon\tau D_1 A_1(t_1)\right)e^{i\omega_1(t_0-\tau)} + \left(\bar{A}_1(t_1) - \varepsilon\tau D_1 \bar{A}_1(t_1)\right)e^{-i\omega_1(t_0-\tau)}, \tag{26}$$

$$x_{20\tau}(t_0, t_1) = \left(A_2(t_1) - \varepsilon\tau D_1 A_2(t_1)\right)e^{i\omega_2(t_0-\tau)} + \left(\bar{A}_2(t_1) - \varepsilon\tau D_1 \bar{A}_2(t_1)\right)e^{-i\omega_2(t_0-\tau)}, \tag{27}$$

$$x_{30\tau}(t_0, t_1) = \psi\left(A_1(t_1) - \varepsilon\tau D_1 A_1(t_1)\right)e^{i\omega_1(t_0-\tau)} + \bar{\psi}\left(\bar{A}_1(t_1) - \varepsilon\tau D_1 \bar{A}_1(t_1)\right)e^{-i\omega_1(t_0-\tau)}. \tag{28}$$

Now, by substituting Eqs (18)–(20), (26)–(28) are inserted into Eqs (15) and (16), the result is:

$$
\begin{aligned}
(D_0^{\,2}+\omega_1^2)x_{11} = &\Big(-2i\omega_1 D_1A_1 + i\tilde{\mu}_1\omega_1A_1 - 3\tilde{\alpha}_1A_1^2\overline{A}_1 - 3i\omega_1^3\tilde{\alpha}_2A_1^2\overline{A}_1 + 2\tilde{\alpha}_3\omega_1^2A_1^2\overline{A}_1\Big)e^{i\omega_1t_0}\\
&+\tilde{\gamma}\psi(A_1-\varepsilon\tau D_1A_1)e^{i\omega_1(t_0-2\tau)} + \tilde{\beta}(A_2-\varepsilon\tau D_1A_2)e^{i\omega_2(t_0-\tau)}\\
&-\Big(\tilde{\alpha}_1A_1^3 - 2\tilde{\alpha}_3\omega_1^2A_1^3\Big)e^{3i\omega_1t_0} + \frac{\Omega^2\tilde{f}}{2}e^{i\Omega t_0} + cc,
\end{aligned}
\tag{29}
$$

$$
(D_0^{\,2}+\omega_2^2)x_{21} = \Big(-2i\omega_2D_1A_2 - i\tilde{\mu}_2\omega_2A_2\Big)e^{i\omega_2t_0} + \tilde{\lambda}(A_1-\varepsilon\tau D_1A_1)^2e^{i\omega_1(t_0-\tau)} + cc, \tag{30}
$$

where cc represents the complex-conjugate term. To achieve a nonsingular solution for Eqs (29) and (30) at the primary with a 1:1 internal resonance, the coefficients of $e^{i\omega_1t_0}$ and $e^{i\omega_2t_0}$, as well as the small divisor, must be nullified. Thus, we can express the relations between Ω, ω_2, and ω_1 as follows:

$$
\Omega = \omega_1 + \varepsilon\tilde{\sigma}_1 = \omega_1 + \sigma_1, \qquad \omega_2 = \omega_1 + \varepsilon\tilde{\sigma}_2 = \omega_1 + \sigma_2. \tag{31}
$$

Here σ_1 and σ_2 are two parameters that represent the difference between Ω, ω_1 and ω_2, respectively. Inserting Eq (31) into Eqs (29) and (30) and removing the resulting singular terms, yields the following solvability constraints:

$$
\begin{aligned}
&\Big(-2i\omega_1D_1A_1 + i\tilde{\mu}_1\omega_1A_1 - 3\tilde{\alpha}_1A_1^2\overline{A}_1 - 3i\omega_1^3\tilde{\alpha}_2A_1^2\overline{A}_1 + 2\tilde{\alpha}_3\omega_1^2A_1^2\overline{A}_1\Big) + \frac{\Omega^2\tilde{f}}{2}e^{i\tilde{\sigma}_1t_0} + \tilde{\gamma}\psi A_1e^{-2i\omega_1\tau}\\
&\qquad + \tilde{\beta}A_{2\tau}e^{-i\omega_2\tau}e^{i\tilde{\sigma}_2t_0} = 0
\end{aligned}
\tag{32}
$$

$$
-2i\omega_2D_1A_2 - i\tilde{\mu}_2\omega_2A_2 + \tilde{\lambda}(A_1-\varepsilon\tau D_1A_1)e^{-i\omega_1\tau}e^{-i\tilde{\sigma}_2t_0} = 0\,. \tag{33}
$$

To derive the averaged equations of the closed-loop control system given by Eqs (2)–(4), we can represent $A_j(t_1)$, $\{j=1,2\}$, in the polar form as follows:

$$
A_1(t_1) = \frac{1}{2}\tilde{a}_1(t_1)e^{i\theta_1(t_1)} \Rightarrow \quad D_1A_1(t_1) = \frac{1}{2}\left(\frac{d}{dt_1}\tilde{a}_1(t_1) + i\tilde{a}_1(t_1)\frac{d}{dt_1}\theta_1(t_1)\right)e^{i\theta_1(t_1)}, \quad a_1 = \varepsilon\tilde{a}_1 \tag{34}
$$

$$
\begin{aligned}
&A_2(t_1) = \frac{1}{2}\tilde{a}_2(t_1)e^{i\theta_2(t_1)} \Rightarrow \quad D_1A_2(t_1) = \frac{1}{2}\\
&\left(\frac{d}{dt_1}\tilde{a}_2(t_1) + i\tilde{a}_2(t_1)\frac{d}{dt_1}\theta_2(t_1)\right)e^{i\theta_2(t_1)}, \quad a_2 = \varepsilon\tilde{a}_2.
\end{aligned}
\tag{35}
$$

From Eqs (34) and (35) into Eqs (32) and (33), we have:

$$
\begin{aligned}
\frac{da_1}{dt} = &\frac{-1}{2}\left(-\mu_1 + \frac{\gamma\delta}{(\rho^2+\omega_1^2)}\cos(2\omega_1\tau) + \frac{\gamma\delta\rho}{\omega_1(\rho^2+\omega_1^2)}\sin(2\omega_1\tau)\right)a_1 - \frac{3}{8}\alpha_2\omega_1^2a_1^3\\
&+\frac{\beta}{2\omega_1}\sin(\varphi_2-\omega_2\tau)a_2 + \frac{\Omega^2f}{2\omega_1}\sin(\varphi_1)
\end{aligned}
\tag{36}
$$

$$\frac{da_2}{dt} = -\frac{\mu_2}{2}a_2 - \frac{\lambda}{2\omega_2}\sin(\varphi_2 + \omega_1\tau)a_1, \tag{37}$$

$$\begin{aligned}\frac{d\varphi_1}{dt} = &\left(\sigma_1 - \frac{\gamma\delta}{2(\rho^2+\omega_1^2)}\sin(2\omega_1\tau) + \frac{\gamma\delta\rho}{2\omega_1(\rho^2+\omega_1^2)}\cos(2\omega_1\tau)\right) + \left(-\frac{3\alpha_1}{8\omega_1} + \frac{\alpha_3\omega_1^2}{4\omega_1}\right)a_1^2 \\ &+ \frac{\beta}{2\omega_1 a_1}\cos(\varphi_2 - \omega_2\tau)a_2 + \frac{\Omega^2 f}{2\omega_1 a_1}\cos(\varphi_1),\end{aligned} \tag{38}$$

$$\begin{aligned}\frac{d\varphi_2}{dt} = &\left(\sigma_2 + \frac{\gamma\delta\rho}{2\omega_1(\rho^2+\omega_1^2)}\cos(2\omega_1\tau) - \frac{\gamma\delta}{2(\rho^2+\omega_1^2)}\sin(2\omega_1\tau)\right) + \frac{\beta}{2\omega_1 a_1}\cos(\varphi_2 - \omega_2\tau)a_2 \\ &- \frac{\lambda}{2\omega_2 a_2}\cos(\varphi_2 + \omega_1\tau)a_1 + \left(-\frac{3\alpha_1}{8\omega_1} + \frac{\alpha_3\omega_1^2}{4\omega_1}\right)a_1^2 + \frac{\Omega^2 f}{2\omega_1 a_1}\cos(\varphi_1).\end{aligned} \tag{39}$$

$\varphi_1 = \sigma_1 t - \theta_1$ and $\varphi_2 = \sigma_2 t + \theta_2 - \theta_1$. To express the closed-form periodic solution of Eqs (2)–(4), let us substitute Eqs (18)–(20), (31), (34), and (35) into Eqs (5)–(7), yield the following:

$$x_1(t) = a_1(t)\cos(\Omega t - \varphi_1(t)), \tag{40}$$

$$x_2(t) = a_2(t)\cos(\Omega t - \varphi_1(t) + \varphi_2(t)), \tag{41}$$

$$x_3(t) = a_3(t)\cos(\Omega t - \varphi_3(t)), \tag{42}$$

where $a_3(t) = \delta a_1(t)/\sqrt{\rho^2 + \omega_1^2}$ and $\varphi_3(t) = \varphi_1(t) - \tan^{-1}(\rho/\omega_1)$. According to Eqs (40) to (42), $a_1(t)$, $a_2(t)$, and $a_3(t)$ denote the oscillation amplitudes of the time-delayed control system and coupled controllers, respectively, while $\varphi_1(t)$, $\varphi_2(t)$, and $\varphi_3(t)$ are the phases of the periodic motions. The slowly varying amplitudes (i.e., $a_1(t)$ and $a_2(t)$) and phases ($\varphi_1(t)$ and $\varphi_2(t)$) are governed Eqs (36)–(39). In addition, $a_3(t) = \delta a_1(t)/\sqrt{\rho^2 + \omega_1^2}$ and $\varphi_3(t) = \varphi_1(t) - \tan^{-1}(\rho/\omega_1)$ are dependent on the $a_1(t)$ and $\varphi_1(t)$. Accordingly, all the dynamics of Eqs (2)–(4) can be explored via analyzing the autonomous system (36) to (39). Therefore, setting $da_1/dt = da_2/dt = d\varphi_1/dt = d\varphi_2/dt = 0.0$ into Eqs (36)–(39), yield the following algebraic system.

$$\begin{aligned}Q_1(a_1, a_2, \varphi_1, \varphi_2) = &\frac{-1}{2}\left(-\mu_1 + \frac{\gamma\delta}{(\rho^2+\omega_1^2)}\cos(2\omega_1\tau) + \frac{\gamma\delta\rho}{\omega_1(\rho^2+\omega_1^2)}\sin(2\omega_1\tau)\right)a_1 \\ &+ \frac{3}{8}\alpha_2\omega_1^2 a_1^3 + \frac{\beta}{2\omega_1}\sin(\varphi_2 - \omega_2\tau)a_2 + \frac{\Omega^2 f}{2\omega_1}\sin(\varphi_1) = 0,\end{aligned} \tag{43}$$

$$Q_2(a_1, a_2, \varphi_1, \varphi_2) = -\frac{\mu_2}{2}a_2 - \frac{\lambda}{2\omega_2}\sin(\varphi_2 + \omega_1\tau)a_1 = 0, \tag{44}$$

$$Q_3(a_1,a_2,\varphi_1,\varphi_2)=\left(\sigma_1-\frac{\gamma\delta}{2(\rho^2+\omega_1^2)}\sin(2\omega_1\tau)+\frac{\gamma\delta\rho}{2\omega_1(\rho^2+\omega_1^2)}\cos(2\omega_1\tau)\right)+\left(-\frac{3\alpha_1}{8\omega_1}+\frac{\alpha_3\omega_1^2}{4\omega_1}\right)a_1^2+\frac{\beta}{2\omega_1 a_1}\cos(\varphi_2-\omega_2\tau)a_2+\frac{\Omega^2 f}{2\omega_1 a_1}\cos(\varphi_1)=0, \tag{45}$$

$$Q_4(a_1,a_2,\varphi_1,\varphi_2)=\left(\sigma_2-\frac{\gamma\delta}{2(\rho^2+\omega_1^2)}\sin(2\omega_1\tau)+\frac{\gamma\delta\rho}{2\omega_1(\rho^2+\omega_1^2)}\cos(2\omega_1\tau)\right)+\frac{\beta}{2\omega_1 a_1}\cos(\varphi_2-\omega_2\tau)a_2-\frac{\lambda}{2\omega_2 a_2}\cos(\varphi_2+\omega_1\tau)a_1+\left(-\frac{3\alpha_1}{8\omega_1}+\frac{\alpha_3\omega_1^2}{4\omega_1}\right)a_1^2+\frac{\Omega^2 f}{2\omega_1 a_1}\cos(\varphi_1)=0. \tag{46}$$

By solving Eqs (43) to (46), simultaneously (i.e., $Q_j(a_1,a_2,\varphi_1,\varphi_2)=0,\ \{j=1,2,3,4\}$), one can plot the oscillation amplitudes of both the self-excited structure (a_1) and the coupled controllers (a_2 and a_3) against the driving frequency Ω in terms of the different control gains (i.e., $\beta,\gamma,\lambda,\rho,$ and δ) as well as the loop delay (τ). In addition, to investigate the solution stability of Eqs (43)–(46), assume the fixed-point solution of these equations is $(a_1,a_2,\varphi_1,\varphi_2)=(h_1,\ h_2,\ h_3,\ h_4)$, and let $(g_1,\ g_2,\ g_3,\ g_4)$ is a small deviation from the fixed-point solution $(h_1,\ h_2,\ h_3,\ h_4)$. Accordingly, we have

$$a_1=h_1+g_1,\ a_2=h_2+g_2,\quad \varphi_1=h_3+g_3,\quad \varphi_2=h_4+g_4\Rightarrow \dot{a}_1=\dot{g}_1,\ \dot{a}_2=\dot{g}_2,\ \dot{\varphi}_1=\dot{g}_3,\ \dot{\varphi}_2=\dot{g}_4. \tag{47}$$

Substituting for $a_1,a_2,\ \varphi_1,$ and φ_2 as defined in Eq (47) into the dynamical system given by Eqs (36)–(39) with linearization about the fixed point $(h_1,\ h_2,\ h_3,\ h_4)$, yields the following variational equations:

$$\dot{g}_1=N_{11}g_1+N_{12}g_2+N_{13}g_3+N_{14}g_4, \tag{48}$$

$$\dot{g}_2=N_{21}g_1+N_{22}g_2+N_{23}g_3+N_{24}g_4, \tag{49}$$

$$\dot{g}_3=N_{31}g_1+N_{32}g_2+N_{33}g_3+N_{34}g_4, \tag{50}$$

$$\dot{g}_4=N_{41}g_1+N_{42}g_2+N_{43}g_3+N_{44}g_4, \tag{51}$$

where $N_{jk},\ \{j=1,2,3,4,\ k=1,2,3,4\}$ are given in appendix. Accordingly, the solution's stability of Eqs (43) to (46) can be determined depending on the eigenvalues of Eqs (48) to (51) [43].

4. Response curves, stability charts, and control performance

Control performance, stability charts, and numerical simulations of the system given by Eqs (2)–(4) are explored in this section. By solving Eqs (43)–(46), one can plot the oscillation amplitudes ($a_1,\ a_2,$ and a_3) against the driving frequency Ω at various feedback gains (λ and δ), control gains (β and γ), driving force (f), and loop-delay (τ). The following actual system parameters are adopted in the current

analysis [30–32,37–40]: $f = 0.01,\ \mu_1 = 0.01,\ \mu_2 = 0.01,\ \omega_1 = \omega_2 = 3.06309,\ \alpha_1 = 14.4108,\ \alpha_2 = 0.05,\ \alpha_3 = 3.2746,\ \rho = \lambda = \delta = \beta = \gamma = 1.0, \sigma_1 = \sigma_2 = 0.0,\ \Omega = \omega_1 + \sigma_1$, and $\tau = 0.0$.

4.1. Uncontrolled structure

The nonlinear characteristics of the studied self-excited structure governed by Eq (2) before control (i.e., at $\beta = \gamma = 0.0$) have been explored through Figures 2–4. In Figure 2, the structure's oscillation amplitude a_1 is plotted versus the driving frequency $\Omega = \omega_1 + \sigma_1$ over the interval $-1 \leq \sigma_1 \leq 1$ when the driving force $f = 0.01$, where σ_1 is utilized throughout the article to represent the closeness of Ω to the structure's natural frequency ω_1. The dotted red line indicates the unstable oscillation, while the solid blue line denotes the stable vibration. Accordingly, one can infer from Figure 2 that the self-excited structure performs stable periodic oscillations when the driving frequency is very close to ω_1 (i.e., when $-0.1 < \sigma_1 < 0.1$); otherwise, the structure will exhibit unstable oscillations. Based on Eq (40), the stability of a_1 indicates periodic oscillations of the studied self-excited structure, while the instability of a_1 implies a nonperiodic response of the structure (where non-periodicity here means that the system may oscillate in one of three motions: quasi-periodic, chaotic, or unbounded oscillations). To validate the accuracy of the analytical solution provided by Eqs (43) to (46), the nonlinear differential equation governing the dynamics of the uncontrolled structure (i.e., Eq (2) when $\beta = \gamma = 0.0$) was solved numerically using MATLAB's ODE45 at three different driving frequencies, $\Omega = \omega_1 + \sigma_1$, with $\sigma_1 1$ set to $-0.2,\ 0.0,$ and 0.4, as depicted in Figure 2. Examination of the figure shows that the structure undergoes quasiperiodic oscillations for $\sigma_1 = -0.2$ and $\sigma_1 = 0.4$, while it exhibits periodic motion for $\sigma_1 = 0.0$, which aligns accurately with the analytical solution obtained.

In Figure 3(a), the structure's dynamics under varying driving force levels f are analyzed, with a_1 plotted against σ_1 for five different values of f. The figure shows that as the driving force increases, the resonant peak of the structure also rises. Concurrently, the frequency range where the system might exhibit unstable motions becomes narrower as f increases. To illustrate this effect, the stability chart of the structure in the $\sigma_1 - f$ plane is presented in Figure 3(b). The chart clearly indicates that increasing f reduces the frequency band where the system may exhibit unstable periodic solutions while expanding the frequency band where the system may show monostable and bistable periodic oscillations. To validate the accuracy of the stability chart presented in Figure 3(b), Figure 4 illustrates the bifurcation diagram for the structure's motion. This diagram is obtained by plotting the projection of the system's steady-state phase trajectory on the $x_1 = \dot{x_1}$ plane while varying σ_1 over the interval $-1 \leq \sigma_1 \leq 1$ at three different driving force levels. Figure 4(a) shows the bifurcation of the structure's motion at $f = 0.01$, while Figures 4(b) and 4(c) depict the bifurcation at $f = 0.03$ and 0.06, respectively. It is evident from Figure 4 that increasing f from 0.01 to 0.03 and then to 0.06 reduces the frequency band where the system exhibits aperiodic motion, which aligns well with the stability chart in Figure 3(b). Additionally, to determine whether the aperiodic response in Figure 4 is quasi-periodic or chaotic, the $0-1$ chaos test is plotted alongside the bifurcation diagrams [44,45]. The test consistently shows a magnitude close to zero, indicating that the aperiodic response is quasi-periodic motion.

So far in the analysis, it can be concluded that the structure under consideration shows unstable oscillations when the driving frequency deviates from the resonant frequency, while it exhibits robust stable oscillations at resonant frequencies. In the subsequent subsection, our goal is to eliminate resonant vibrations and stabilize the system's motion, regardless of the driving force amplitude or frequency, whether it is near or far from the system's natural frequency.

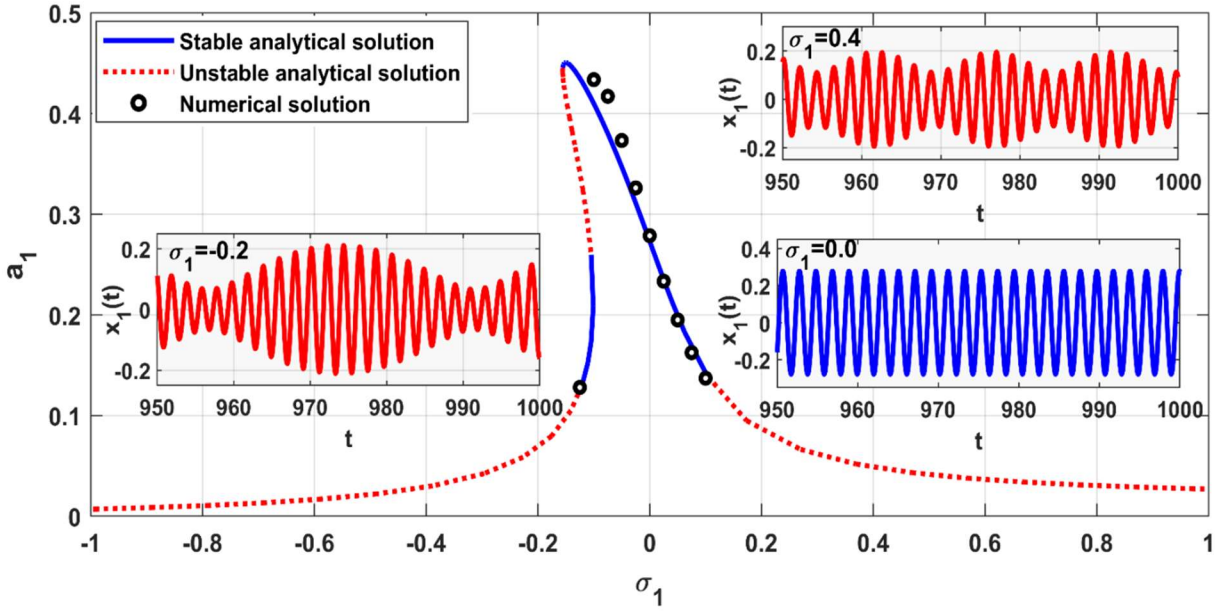

Figure 2. Self-excited structure without control: a_1 against the driving frequency $\Omega = \omega_1 + \sigma_1$, and the corresponding time response when $\sigma_1 = -0.2, 0.0,$ and 0.4.

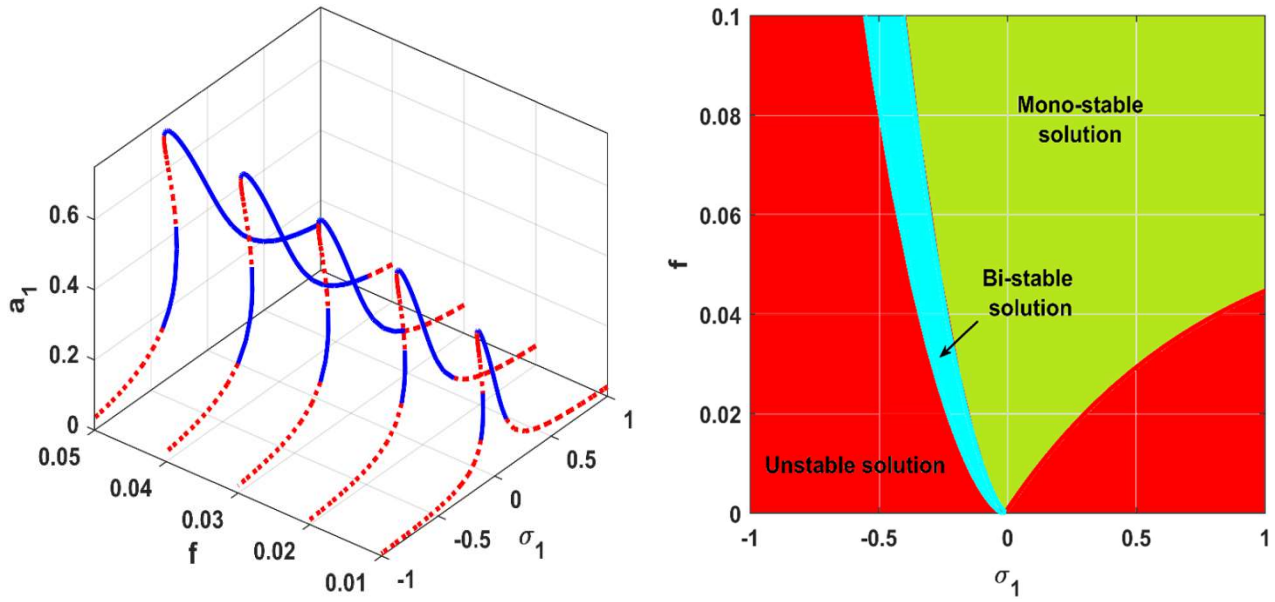

Figure 3. Self-excited structure without control: (a) a_1 against σ_1 at different values of f, (b) chart of stability in $\sigma_1 - f$ plane.

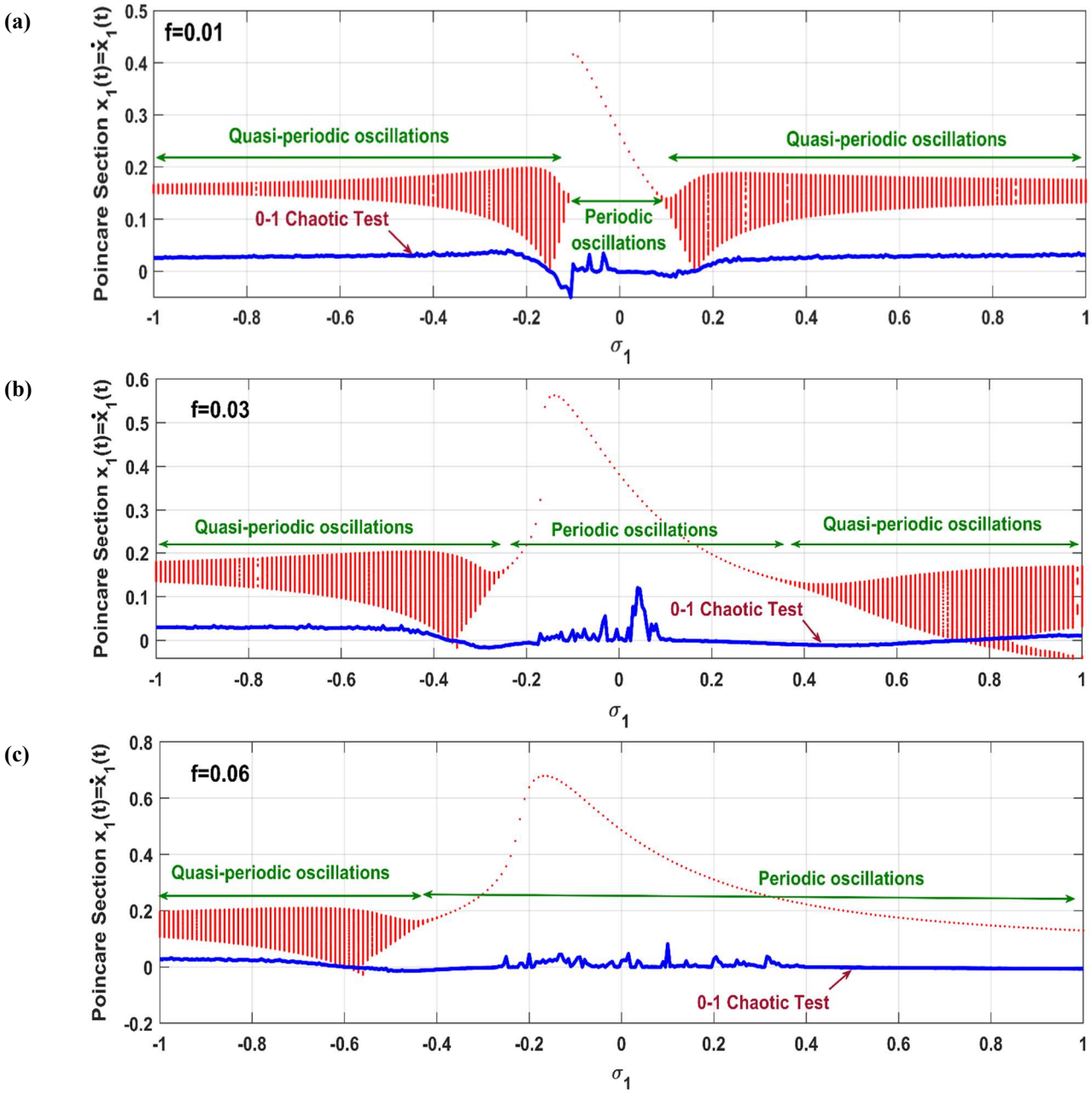

Figure 4. Uncontrolled structure bifurcation diagram: (a) Poincaré section $x_1 = \dot{x_1}$ and the corresponding 0-1 chaotic test against σ_1 when $f = 0.01$, (b) Poincaré section $x_1 = \dot{x_1}$ and the corresponding 0-1 chaotic test against σ_1 when $f = 0.03$, and (b) Poincaré section $x_1 = \dot{x_1}$ and the corresponding 0-1 chaotic test against σ_1 when $f = 0.06$.

4.2. Dynamics of the non-delayed control system

In this sub-section, the dynamics of the self-excited structure under the proposed control strategy are examined, excluding the loop delay. Initially, the impact of coupling the second-order filter described by Eq (3) to the self-excited structure is analyzed by solving Eqs (43) to (46) (with $\gamma = \delta = \tau = 0$), as illustrated in Figures 5–7. Figures 5(a) and 5(b) display oscillation amplitudes of the structure (a_1) and the coupled second-order filter (a_2) plotted against σ_1 at various driving force

levels f when $\beta = \lambda = 1.0$.

Firstly, the figures indicate that coupling the structure to a second-order filter with the same natural frequency as the main system (i.e., $\omega_1 = \omega_2$) establishes an energy transfer between the two subsystems. This results in the vibration energy of the structure being transferred to the filter when $\Omega = \omega_1 = \omega_2$, causing the oscillation amplitude of the main structure to approach zero at $\sigma_1 = 0$. Secondly, while coupling the second-order filter stabilizes the system's quasiperiodic oscillation at a low driving force (i.e., $f = 0.01$), an increase in f may lead to unstable motion of the controlled structure when the driving frequency is below the structure's natural frequency, as shown in the stability chart in Figure 5(c) that is not the case of the uncontrolled structure demonstrated in the chart of stability given in Figure 3(b). This contrasts with the behavior of the uncontrolled structure, as demonstrated in the chart of stability in Figure 3(b), where an increase in the driving force destabilizes the stable motion of the controlled structure while increasing the driving force stabilizes the unstable motion of the uncontrolled structure.

Extensive analytical and numerical investigations have revealed that the efficiency of the coupled second-order filter in riding off the vibration of the self-excited structure depends not on the magnitude of β or λ independently, but on their algebraic product, as shown in Figure 6(a). The figure depicts the oscillation amplitudes of the controlled structure when $\beta\lambda = 4.0$, regardless of the individual values of β and λ. However, Figure 6(b) demonstrates that the oscillation amplitude of the coupled second-order filter does not depend on the algebraic product of β and λ, but on their values individually. Two combinations of β and λ have been selected such that $\beta\lambda = 4.0$: The first one is $\beta = 4.0$ and $\lambda = 1.0$, while the second one is $\beta = 1.0$ and $\lambda = 4.0$. Figure 6(b) clearly shows that the oscillation amplitude of the controller increases monotonically with λ and decreases monotonically with β. To illustrate this phenomenon, the vibration amplitudes of both the structure (a_1) and the controller (a_2) have been plotted against σ_1 at six different values of $\beta\lambda$ (i.e., $\beta\lambda = 1, 2, \dots, 6$), along with the corresponding stability chart in $\sigma_1 - \beta\lambda$ plane, as shown in Figure 7. Figure 7(a),(b) show that the structure's vibration amplitude and the stability charts depend on the magnitude of the algebraic product of β and λ, regardless of the individual values of each. However, Figures 7(c),(d) demonstrate that a_2 is a monotonic decreasing function of β when λ is fixed, and a monotonic increasing function of λ when β is fixed. Therefore, in the rest of the analysis, $\beta\lambda$ has been treated as a single control parameter, with λ fixed to the neutral value (i.e., $\lambda = 1.0$).

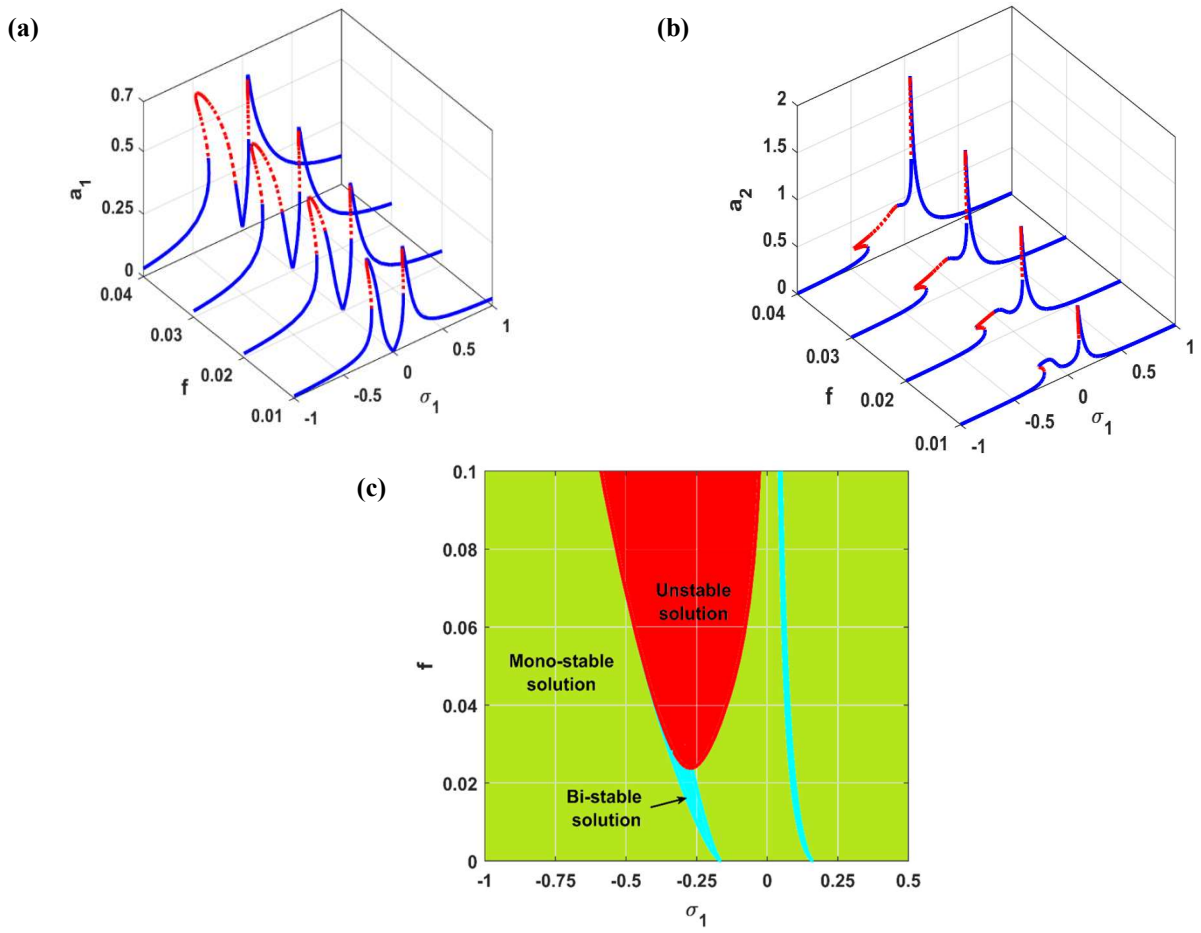

Figure 5. Self-excited structure with control when $\gamma = \delta = 0$ and $\beta = \lambda = 1.0$: (a,b) vibration amplitudes against σ_1 at different driving forces, and (c) the corresponding stability chart in $\sigma_1 - f$ plane.

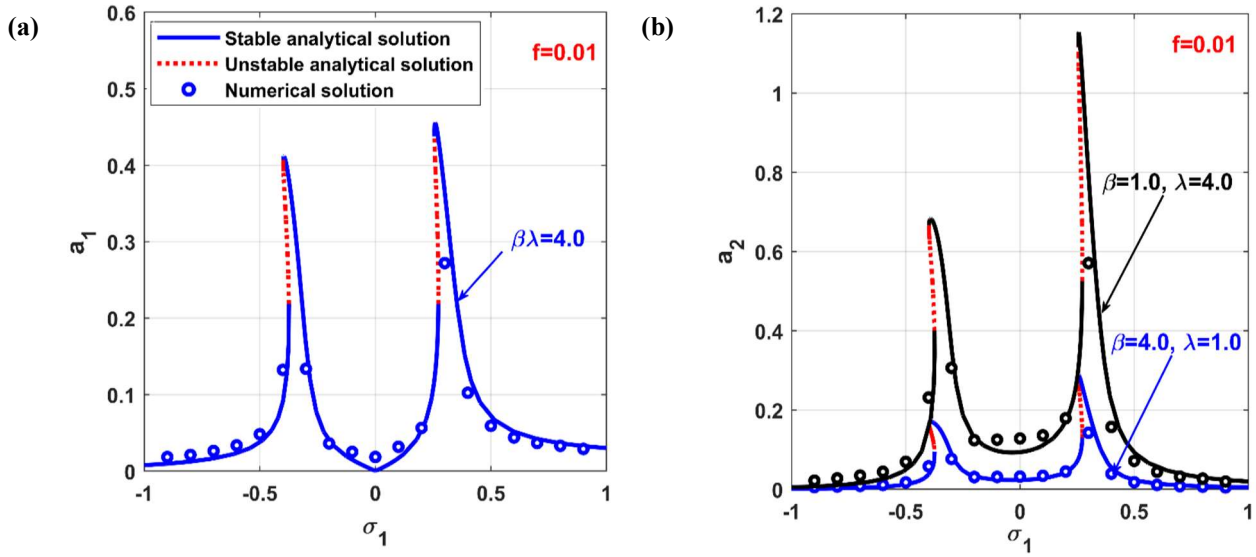

Figure 6. Analytical solution versus numerical simulation of the controlled system when $\gamma = \delta = 0$and $f = 0.01$: (a) a_1 against σ_1, (b) a_2 against σ_1.

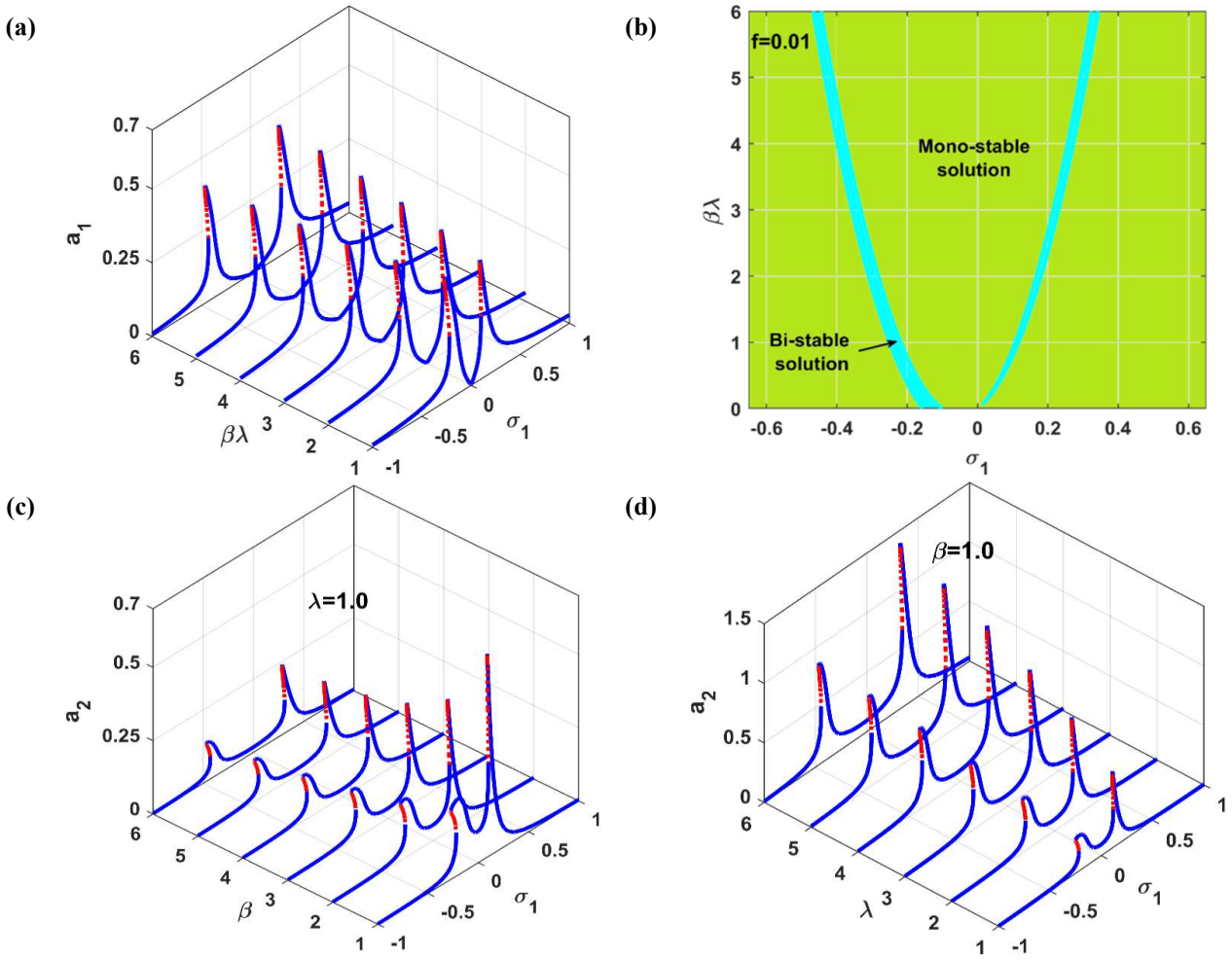

Figure 7. Self-excited structure with control when $\gamma = \delta = 0$ and $f = 0.01$: (a) structure vibration amplitude against σ_1 at different control gains $\beta\lambda$, (b) stability chart in $\sigma_1 - \beta\lambda$ plane, (c) controller vibration amplitude against σ_1 at various levels of β when $\lambda = 1.0$, (d) controller vibration amplitude against σ_1 at various levels of λ when $\beta = 1.0$.

The influence of the first-order filter described by Eq (4) on the dynamics of the self-excited structure is analyzed in Figures 8 and 9 by solving Eqs (43) to (46) when effectively decoupling the second-order filter by setting $\beta = \lambda = 0.0$. Notably, the control and feedback gains of the coupled first-order filter (γ and δ)) appear in Eqs (43) to (46) as an algebraic product. This implies that the controller's efficiency relies on the product of γ or δ, than on these parameters independently. Figure 8(a),(b) display the vibration amplitudes of the structure (a_1) and the first-order filter (a_3) plotted against σ_1 for $\gamma\delta$ values of 0.0, 0.25, 0.5, 0.75, and 1.0. The chart of stability in the $\sigma_1 - \gamma\delta$ plane, shown in Figure 8(c), clearly illustrates that increasing $\gamma\delta$ riding off the nonlinear bifurcations of the self-excited structure, such as bi-stability and jump phenomena, and stabilizes the structure's motion. However, regardless of the magnitude of the control key $\gamma\delta$, the system exhibits maximum vibration amplitudes at perfect resonance conditions (i.e., when $\sigma_1 = 0.0$). The influence of the control parameter ρ on the structure's oscillatory behavior is depicted in Figure 9. Figure 9(a), (b) demonstrate that the structure's amplitude of oscillation is a monotonically increasing function of ρ, which contrasts with the effect of increasing the control key $\gamma\delta$. The chart of stability in Figure 9(c) shows that the stable motion of the structure at $\rho = 0.0$ along the σ_1 axis can become unstable as ρ is increased to 15. The positive effect of $\gamma\delta$ and the

negative effect of ρ on vibration suppression efficiency and closed-loop stability can be understood through the derived autonomous differential equation (36). The coefficient a_1 in Eq (36) represents the equivalent damping of the controlled structure ($\mu_e = \gamma\delta/(\rho^2 + \omega_1^2)$ when $\tau = 0.0$. It is evident that equivalent damping is directly proportional to $\gamma\delta$ and inversely proportional to ρ^2. This explains why increasing $\gamma\delta$ and/or decreasing ρ can enhance the self-excited structure's dynamic characteristics. Based on the results from Figures 8 and 9, it can be concluded that coupling a first-order filter to the self-excited structure effectively achieves the system's stability. However, complete elimination of the structure's vibrations remains

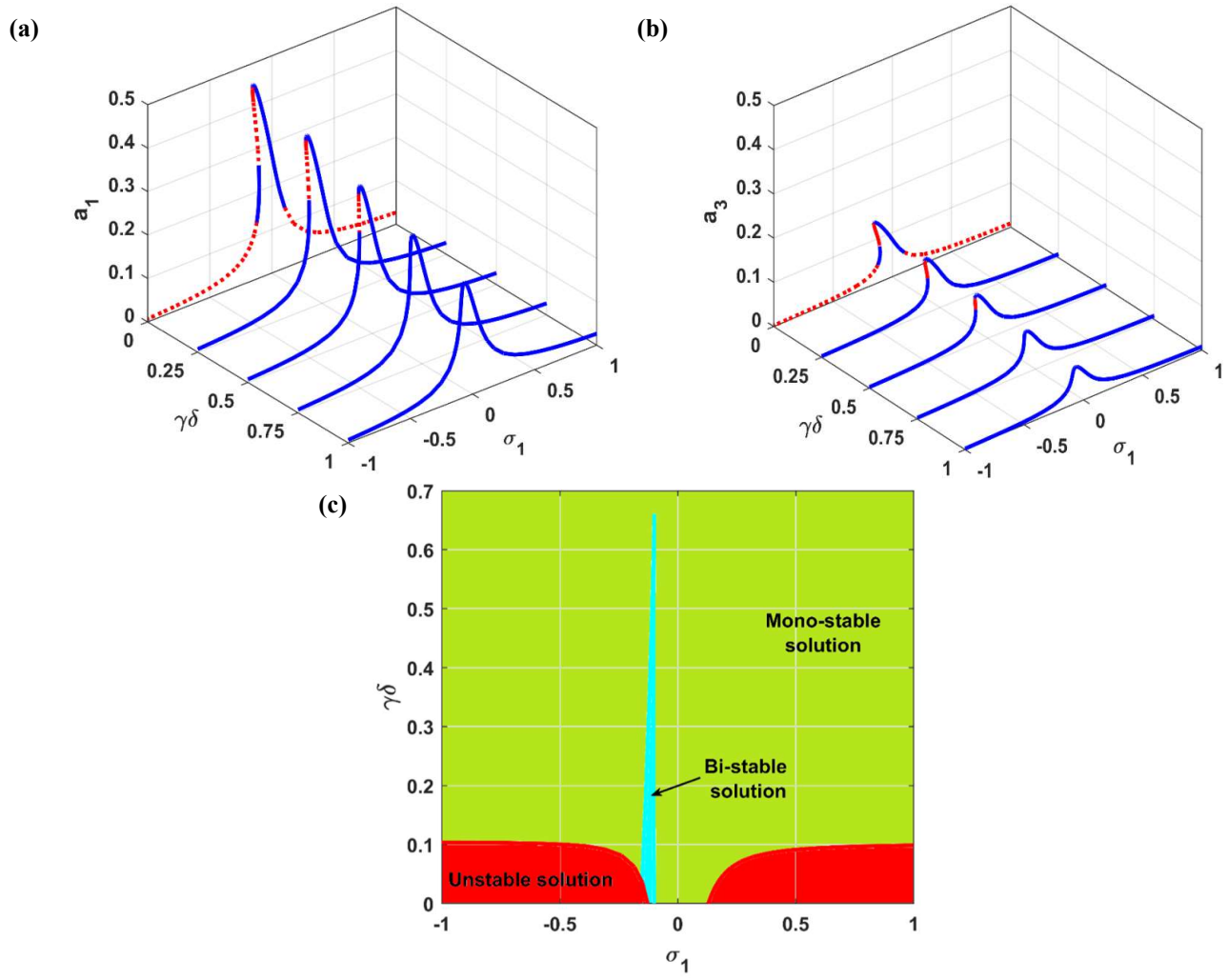

Figure 8. Self-excited structure with control when $\beta = \lambda = 0.0$ and $f = 0.01$: (a, b) vibration amplitudes against σ_1 at different control gains $\gamma\delta$, and (c) chart of stability in $\sigma_1 - \gamma\delta$ plane.

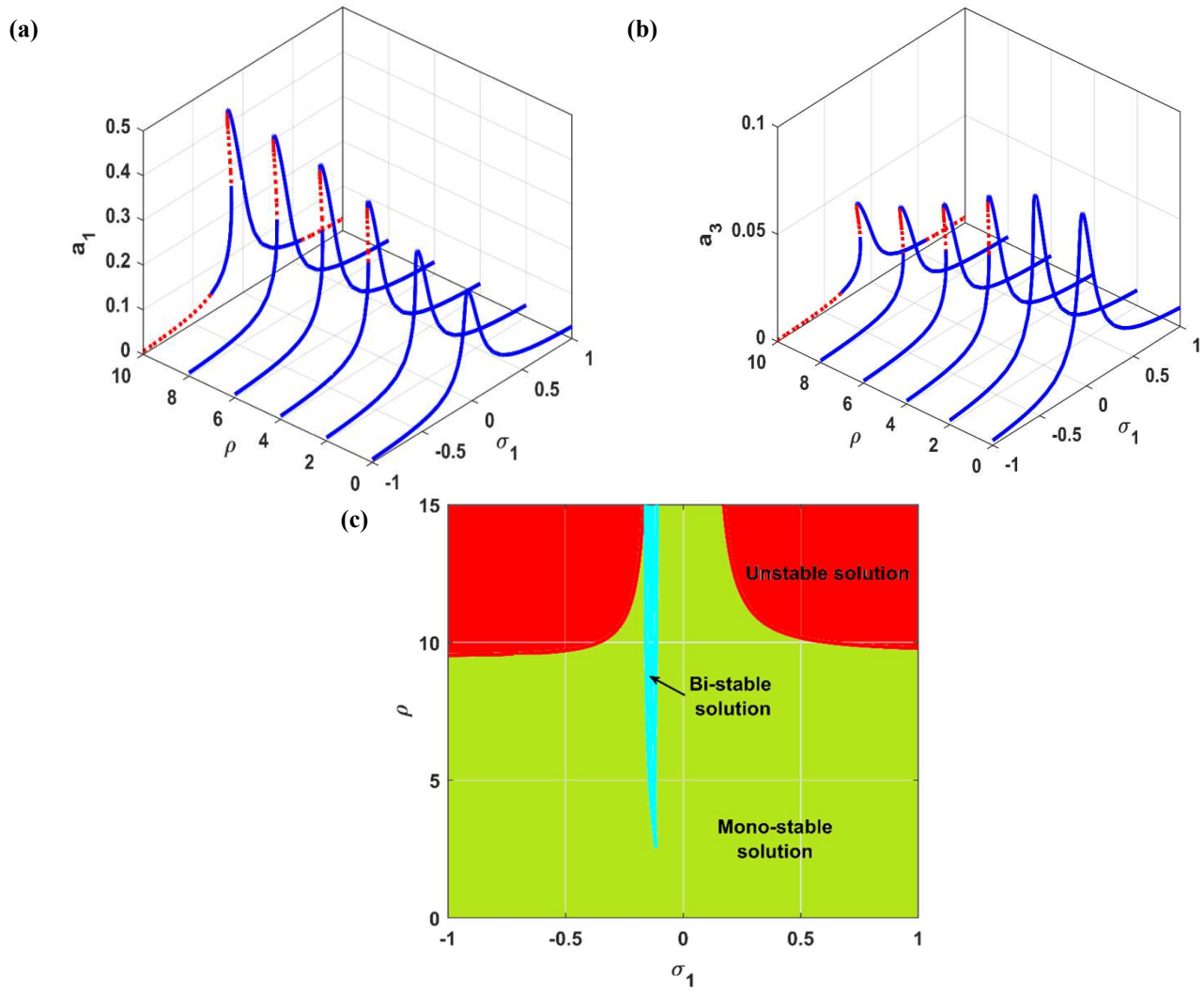

Figure 9. Self-excited structure with control when $\beta\lambda = 0.0$, $\gamma\delta = 1.0$ and $f = 0.01$: (a, b) vibration amplitudes against σ_1 at different values of ρ, and (c) chart of stability in $\sigma_1 - \rho$ plane.

Finally, Figure 10 illustrates how the second-order filter effectively creates an energy link between the self-excited structure and the controller, allowing control of the vibration elimination bandwidth through β. Additionally, it shows how the first-order filter contributes to stabilizing the structure's unstable motion and enhancing the closed-loop damping coefficient. This analysis is conducted at five different values of $\gamma\delta$ with $\beta = 2.0$ and $\lambda = 1.0$. The figure shows that the combined controller, optimized with parameter values $\beta = 2.0, \lambda = 1.0,$ and $\gamma\delta = 4.0$, not only stabilizes and eliminates the nonlinear oscillations of the structure but also ensures that the two filters exhibit minimal oscillation amplitudes (i.e., a_2 and a_3 remain small). This confirms the practical viability of this control strategy.

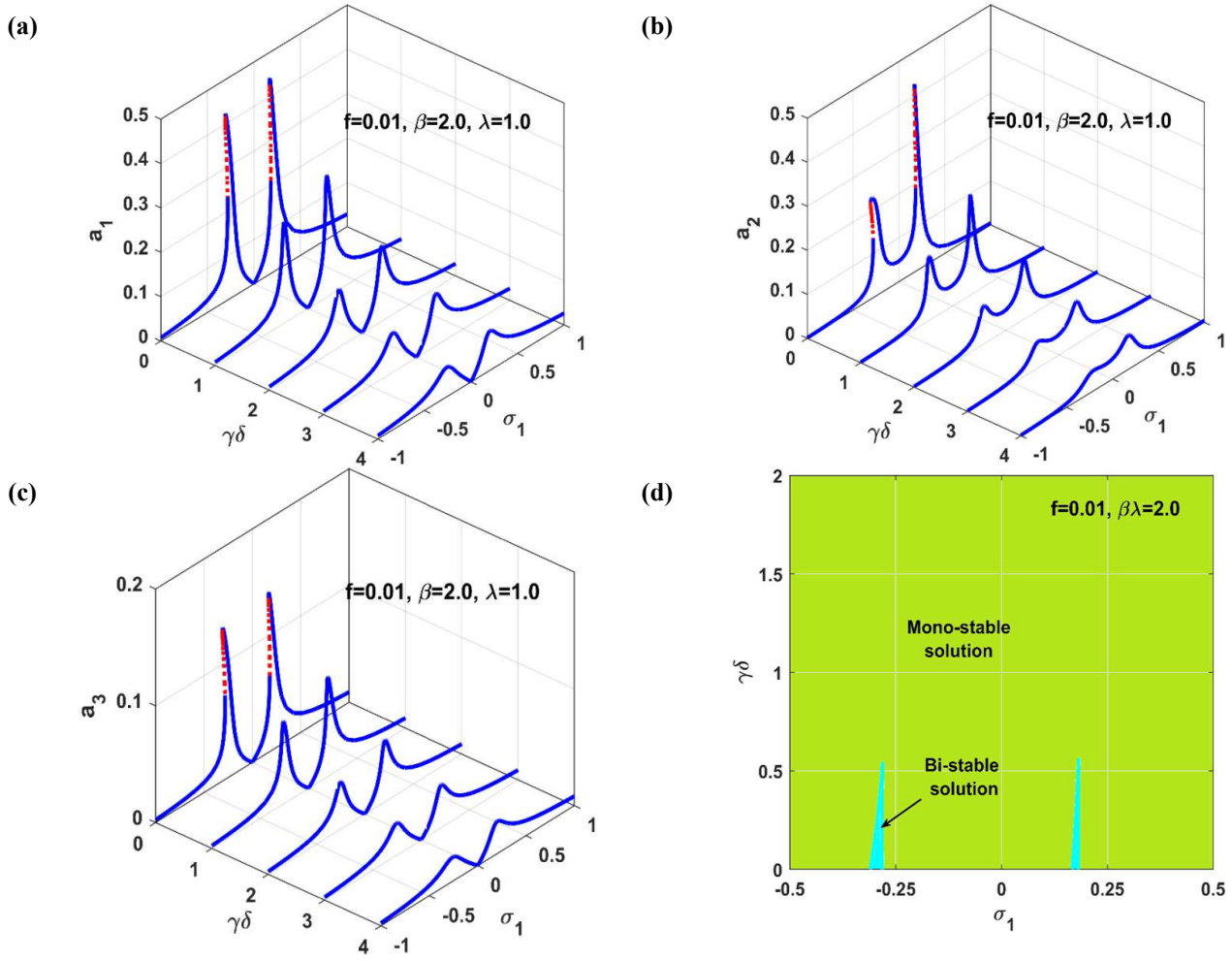

Figure 10. Self-excited structure with control when $\beta\lambda = 2.0$ and $f = 0.01$: (a, b, c) vibration amplitudes against σ_1 at different control gains $\gamma\delta$, and (c) chart of stability in $\sigma_1 - \gamma\delta$ plane.

To demonstrate the effectiveness of the combined controller, Figure 11 compares the response curve of the uncontrolled structure with that of the controlled structure (using $\beta = 2.0, \lambda = 1.0,\ \gamma\delta = 4.0$). The analytical solution (solid and dotted lines), obtained by solving Eqs (43) to (46), is plotted alongside the numerical solution obtained by solving Eqs (2) to (4) with the ODE45 MATLAB solver for $\tau = 0.0$. The figure highlights the excellent agreement between the analytical and numerical solutions. In addition, Figure 11(a) illustrates that the stable, strong vibrations of the uncontrolled structure near perfect resonance (i.e., when σ_1 is close to zero) are effectively eliminated in the controlled structure. This is achieved by channeling the excess vibration energy to the coupled filters, as depicted in Figures 11(b),(c). Furthermore, the unstable motion of the uncontrolled structure, shown in Figure 11(a), is stabilized under control, maintaining minimal oscillation amplitudes. This demonstrates the efficacy and robustness of this controller. Moreover, the bifurcation diagram of the studied structure before and after control has been established, as shown in Figures 12(a),(b), respectively. By comparing these two figures (i.e., Figures 12(a),(b)), one can infer that the quasiperiodic response on both sides of $\sigma_1 = 0.0$ in the uncontrolled system has been transformed after control into periodic monostable motion along the σ_1 axis. Additionally, the basin of attraction

of the system before and after control according to Figure 11(a) when $\sigma_1 = 0.11$, has been constructed, as illustrated in Figures 12(c),(d), respectively. In these figures, the bistable solution before control (Figure 12(c)) has merged into a monostable solution after control, as Figure 12(d) shows.

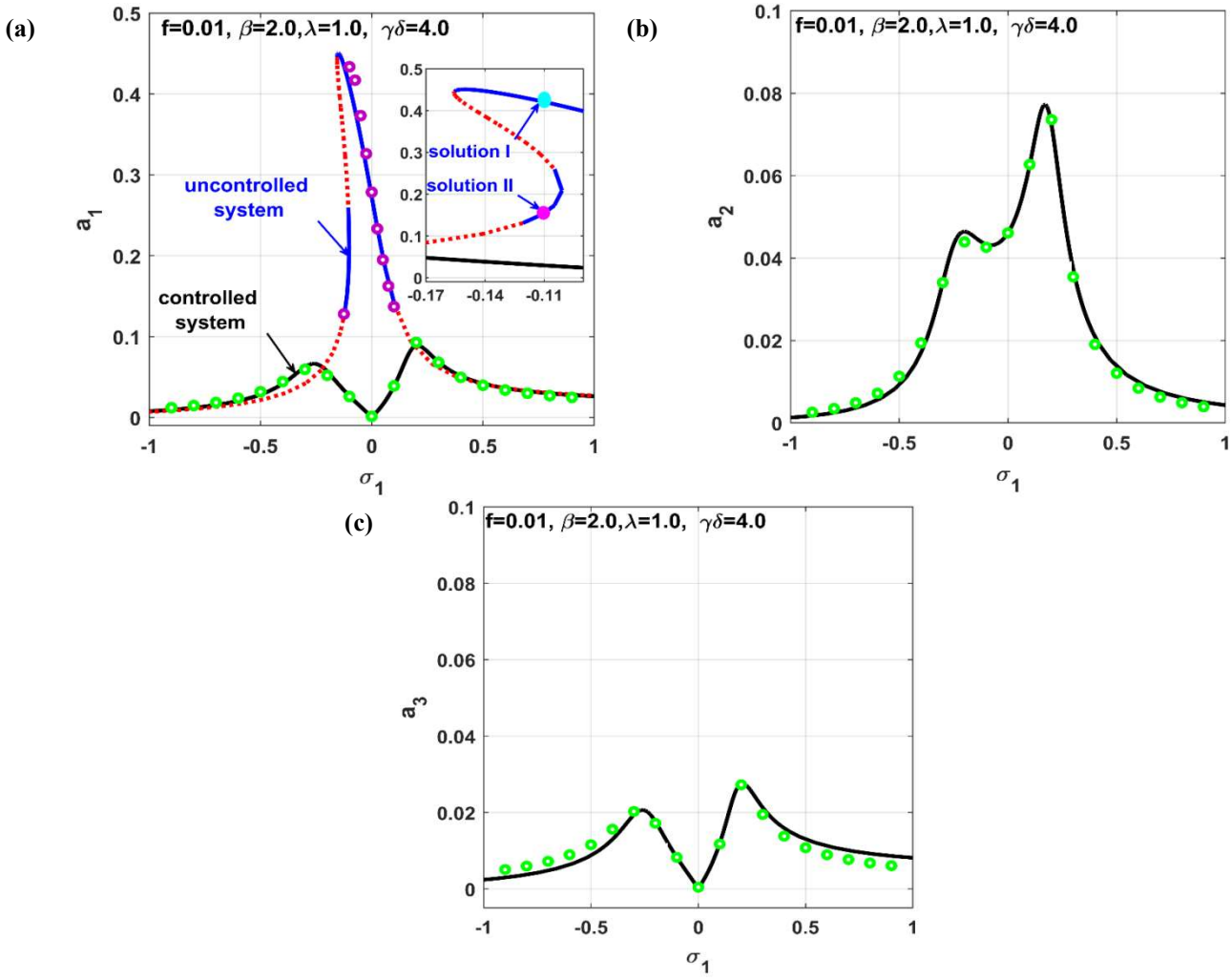

Figure 11. Analytical solution versus numerical simulation of the self-excited structure without control (i.e., $= \beta = \lambda = 0.0$) and with control (i.e., $\gamma\delta = 4.0, \beta = 2.0, \lambda = 1.0$): (a) oscillation amplitude of the structure (a_1) before and after control against σ_1, (b) oscillation amplitude of the second-order filter (a_2) against σ_1, and (c) oscillation amplitude of the first-order filter (a_3) against σ_1.

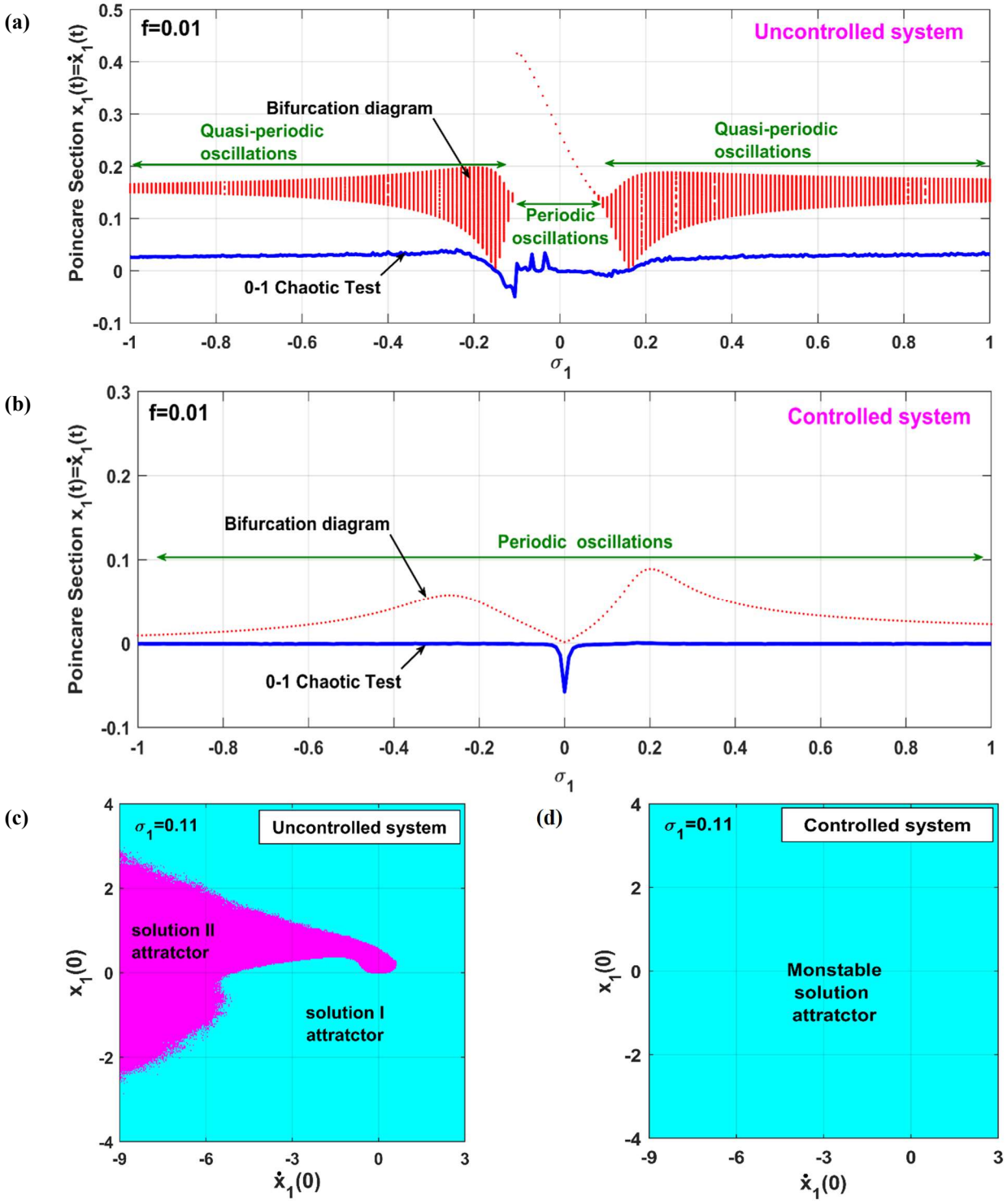

Figure 12. (a) System bifurcation diagram without control (i.e., $= \beta = \lambda = 0.0$), (b) system bifurcation diagram with control (i.e., $\gamma\delta = 4.0, \beta = 2.0, \lambda = 1.0$), (c) basin of attraction without control (i.e., $\delta = \beta = \lambda = 0.0$), and (d) basin of attraction with control (i.e., $\gamma\delta = 4.0, \beta = 2.0, \lambda = 1.0$).

To simulate the oscillation of the structure before and after applying control, corresponding to the response curves in Figures 11 and 12, Eqs (2) to (4) were solved using the MATLAB solver ODE45. Initially, the system oscillation was simulated without control (i.e., $= \beta = \lambda = 0$) over the time interval $0 \leq t < 250$, the control action was applied (i.e., setting $\gamma\delta = 4.0,\ \beta = 2.0,\ \lambda = 1.0$), and the simulation continued until $t = 320$, as depicted in Figures 13 and 14. Figure 13 shows the instantaneous motion of the self-excited structure and the coupled filters under perfect resonance conditions (i.e., $\Omega = \omega_1, \sigma_1 = 0.0$), while Figure 14 presents the system dynamics when $\sigma_1 = 0.5$. In Figure 13(a), the application of the control action quickly reduces the stable high resonant vibrations of the system to near zero. Figure 14(a) illustrates that the control force, applied at $t = 250$, stabilizes the low-amplitude unstable motion of the structure into periodic oscillations, closely matching the analytical results in Figure 11(a). Additionally, Figures 13(b),(c), 14(b), (c) demonstrate that the two filters maintain minimal oscillation amplitudes (i.e., a_2 and a_3 remain small), confirming the practical effectiveness of this control strategy.

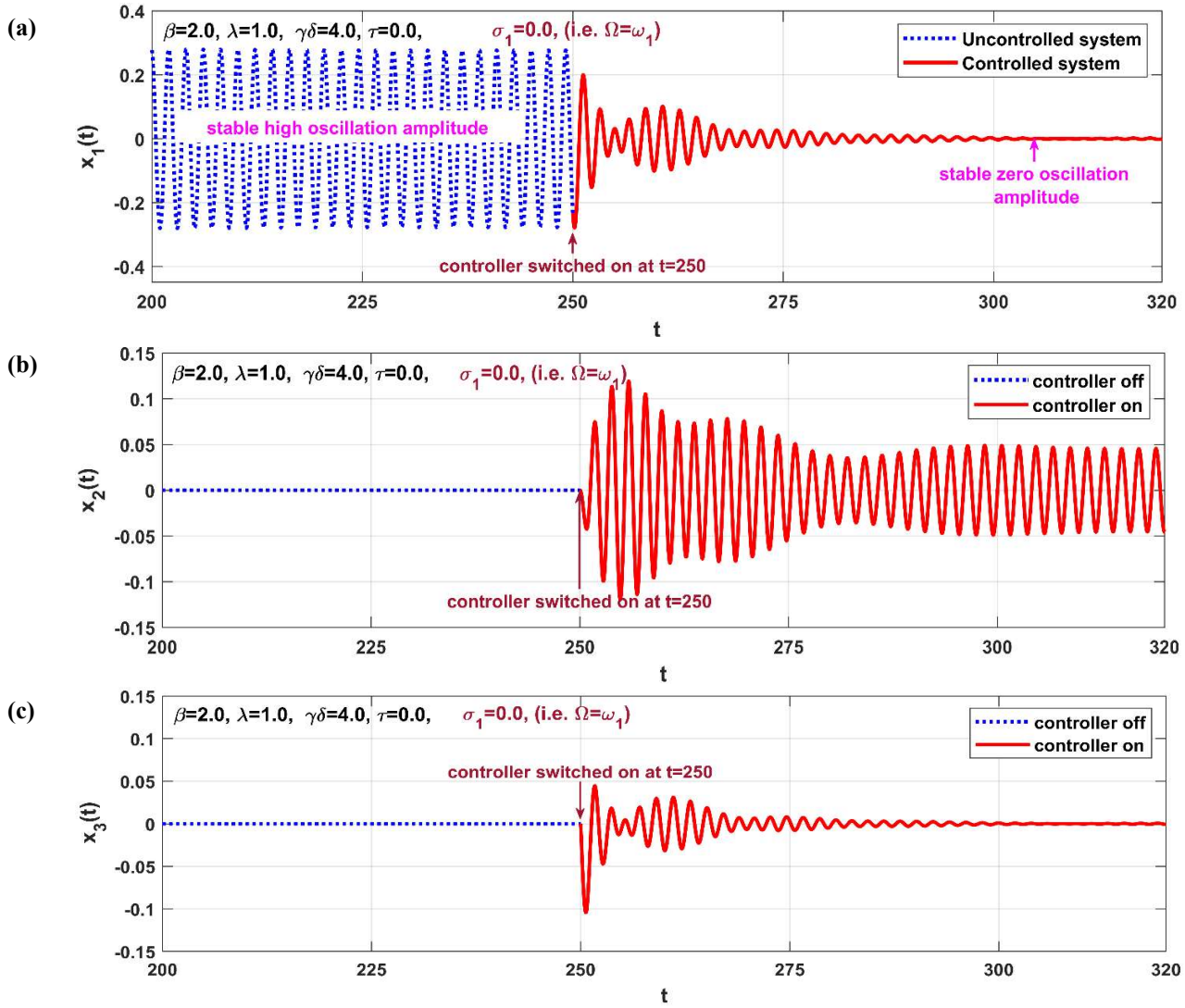

Figure 13. Structure time-response before and after switching the controller on with control gains selected according to Figures 11 and 12 when $\sigma_1 = 0$ (i.e., $\beta\lambda = 2.0,\ \gamma\delta = 4.0,\ \tau = 0$): (a) Time-response of the self-excited structure and (b,c) Time-response of the connected controllers.

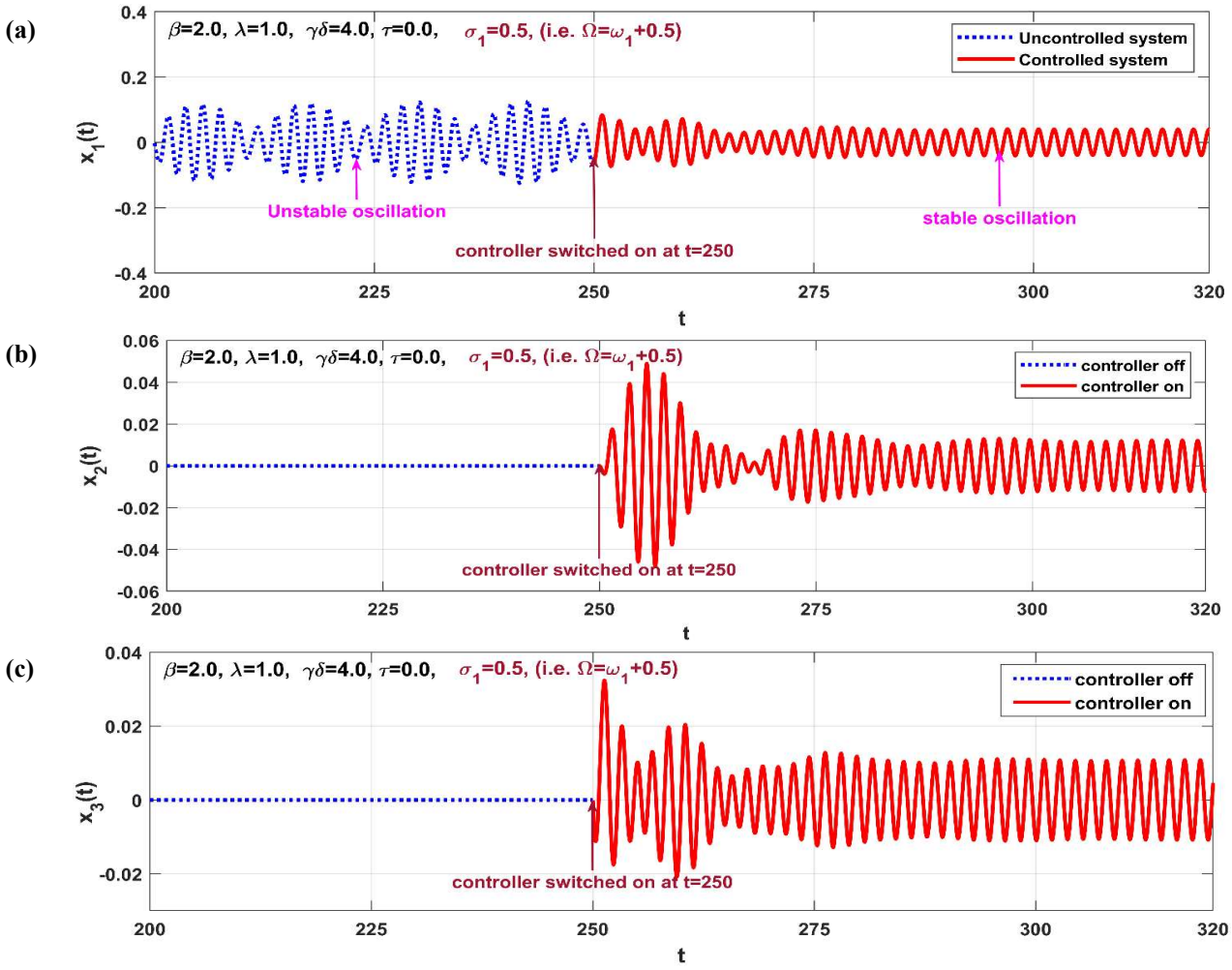

Figure 14. Structure time-response before and after switching the controller with control gains selected according to Figures 11 and 12 when $\sigma_1 = 0.5$ (i.e., $\beta\lambda = 2.0$, $\gamma\delta = 4.0$, $\tau = 0$): (a) Time-response of the self-excited structure and (b, c) Time-response of the connected controllers.

4.3. Loop delay stability margin

In practical applications, measuring the displacement $x_1(t)$ of the self-excited structure using a position sensor, processing the measured signal, computing the control signal, and applying the control action to mitigate undesired oscillations, as illustrated in Figure 1, cannot occur instantaneously. This inherent delay, known as the time-delay phenomenon, is present in any digital closed-loop control system. In this section, we investigate the impact of the loop delay $\tau \neq 0.0$ on both the stability charts and the overall performance of the applied control strategy. As illustrated in the previous subsection, the charts of stability and the oscillation amplitudes of the structure do not depend on the individual values of the parameters β, γ, λ, and δ, but on their algebraic products $\beta\lambda$ and $\gamma\delta$. Accordingly, $\beta\lambda$ and $\gamma\delta$ are treated as two independent parameters alongside the other control keys.

In Figure 15(a), the stability chart of the time-delayed closed-loop system in the $\tau - \beta\lambda$ plane has been established at three values of the control key $\gamma\delta$. It is clear from the figure that the stability margin of the loop delay is inversely proportional to the control key $\beta\lambda$ in a nonlinear fashion, where

an increase in $\beta\lambda$ reduces the stability margin of τ at an apparently exponential decay rate. At the same time, the figure demonstrates that this decay due to an increase in $\beta\lambda$ can be compensated by increasing the control gain $\gamma\delta$. Conversely, Figure 15(b) depicts the loop-delay stability margin against the control key $\gamma\delta$ when $\beta\lambda = 1.0,\ 2.0,$ and 4.0. The figure shows that the stability margin of the closed-loop system increases at an apparently exponential rate with the increase in $\gamma\delta$. However, an increase in the second-order filter gain $\beta\lambda$ narrows the loop stability margin. Based on the results drawn from Figure 15, it can be concluded that loop delay does not pose a significant challenge in the proposed control method. The adverse effects of increasing $\beta\lambda$, which reduces the stability margin and may destabilize the control loop, can be countered by increasing the control key $\gamma\delta$.

To verify the accuracy of the stability charts shown in Figure 15, the time-delayed closed-loop control system described by Eqs (2) to (4) was numerically simulated using the DDE23 MATLAB solver [46]. The simulations, illustrated in Figure 16, were conducted for $\gamma\delta = 1.0, 2.0,$ and 4.0 according to the marked point $\mathrm{P}(\beta\lambda, \tau) = (2.0, 0.05)$ in Figure 15(a). Initially, the system's temporal oscillations were simulated over the interval $0 \le t < 500$ with $\gamma\delta = 1.0$. At $t = 500$, the control key $\gamma\delta$ was increased to 2.0, and the simulation continued until $t < 800$. Subsequently, at $t = 800$, $\gamma\delta$ was further increased to 4.0, with the simulation extending until $t = 1000$. As shown in Figure 16, during the interval $0 \le t < 500$ (where $\gamma\delta = 1.0$), the system displays unstable, growing oscillations when $\gamma\delta = 1.0$, which aligns with the stability chart at point P in Figure 15(a). Furthermore, the system exhibits very small, stable periodic oscillations during the intervals $500 \le t < 800$ (where $\gamma\delta = 2.0$) and $800 \le t \le 1000$ (where $\gamma\delta = 4.0$), accurately reflecting the stability characteristics depicted at point P in Figure 15(a) when $\gamma\delta = 2.0$ or 4.0. In Figure 15(a), the marked point $\mathrm{P}(\beta\lambda, \tau) = (2.0, 0.05)$ demonstrates that the time-delayed system remains stable as long as the control gain $\gamma\delta$ is 4.0 or 2.0. However, decreasing $\gamma\delta$ to 1.0 results in the instability of the closed-loop system. This observation agrees excellently with the numerical simulation presented in Figure 16, underscoring the high accuracy of the established stability charts in Figure 15.

In Figure 17(a), the stability chart in the $\tau - \rho$ space is shown for three different values of the control key $\beta\lambda$. The figure clearly indicates that the loop-delay stability margin is inversely proportional to ρ in a nonlinear manner; as ρ increases, the stability margin of τ decreases. However, this reduction in stability margin due to an increase in ρ can be further increased when $\beta\lambda$ is also increased. Conversely, Figure 17(b) illustrates the loop-delay stability margin against the control key ρ for $\gamma\delta = 1.0,\ 2.0,$ and 4.0. Even though an increase in ρ reduces the stability margin of τ, this adverse effect can be compensated by increasing the control gain $\gamma\delta$.

To illustrate the negative impact of increasing the control key $\beta\lambda$ on the stability of the time-delayed closed-loop control system, as shown in Figure 17(a), the system's time response from Eqs (2) to (4) have been plotted using the DDE23 algorithm for the marked point $\mathrm{P}(\rho, \tau) = (2.0, 0.025)$ at three different values of $\beta\lambda$. For Figure 18, the system's temporal oscillations were simulated over the interval $0 \le t < 300$ with $\beta = \lambda = 1.0$. At $t = 300$, the control gain β was increased to 2.0, and the simulation continued until $t < 800$. Subsequently, at $t = 800$, β was further increased to 4.0, with the simulation extending until $t = 1000$. The figure shows that the system maintains stable, decaying periodic motion during the intervals $0 \le t < 300$ (where $\beta = 1.0$) and $300 \le t < 800$ (where $\beta = 2.0$). However, during the interval $800 \le t \le 1000$ (where $\beta = 4.0$), the system displays unstable, growing oscillations. It is noted that the marked point $\mathrm{P}(\rho, \tau) = (2.0, 0.025)$ in Figure 17(a) indicates that the time-delayed system is stable when $\beta\lambda$ is equal to $= 1.0$ or 2.0. However, if $\beta\lambda$ is increased to 4.0, this implies instability of the closed-loop system, which is in excellent agreement with the numerical simulation shown in Figure 18. This ensures the high accuracy of the established stability charts in Figure 17.

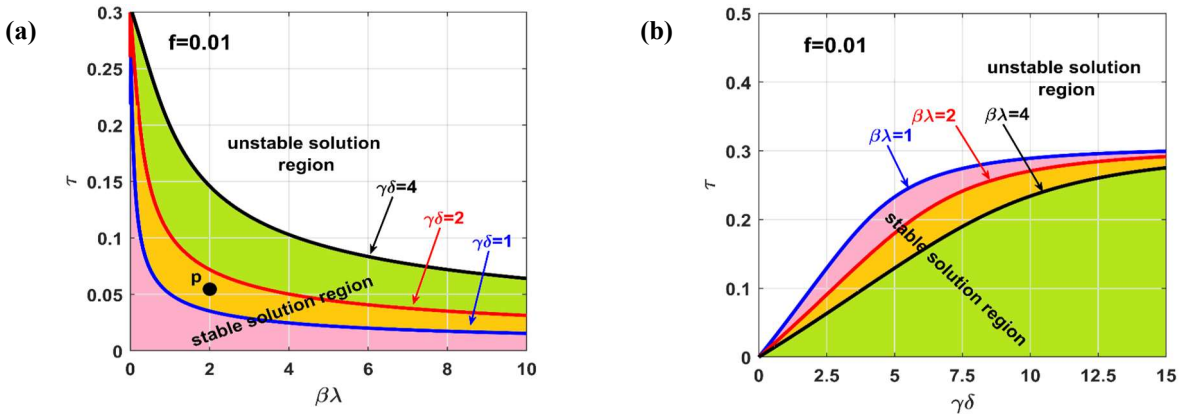

Figure 15. Stability margin of the loop-delay τ against the control gains $\beta\lambda$ and $\gamma\delta$: (a) stability margin of τ against $\beta\lambda$ at various values of $\gamma\delta$, and (b) stability margin of τ against $\gamma\delta$ at various values of $\beta\lambda$.

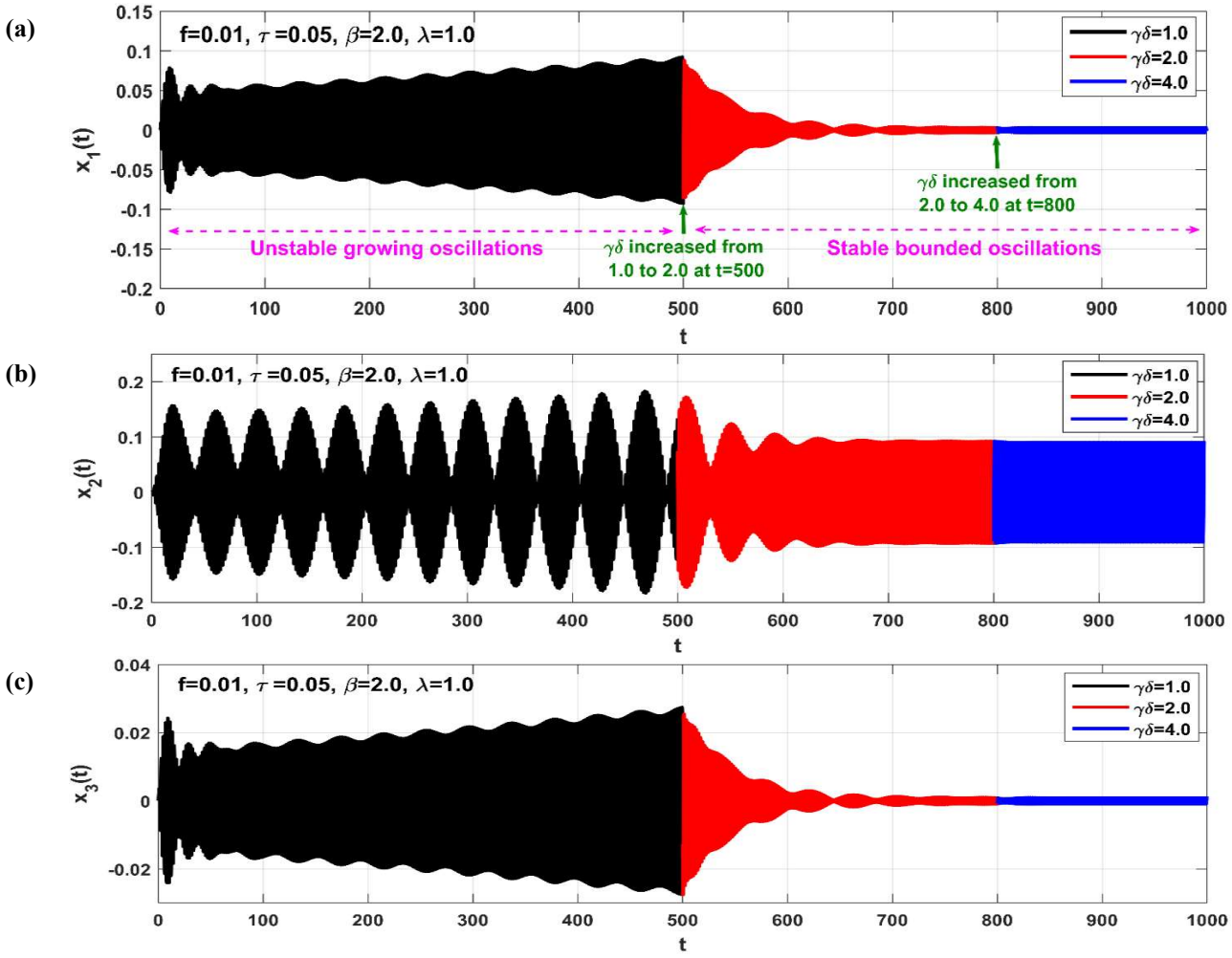

Figure 16. Controlled structure time-response corresponding to the marked point P (i.e., when $\tau = 0.05$ and $\beta\lambda = 2.0$) shown on the stability chart in Figure 15(a) when $\gamma\delta$ is increased from 1.0 to 2.0 at $t = 500$, and then further increased from 2.0 to 4.0at $t = 800$.

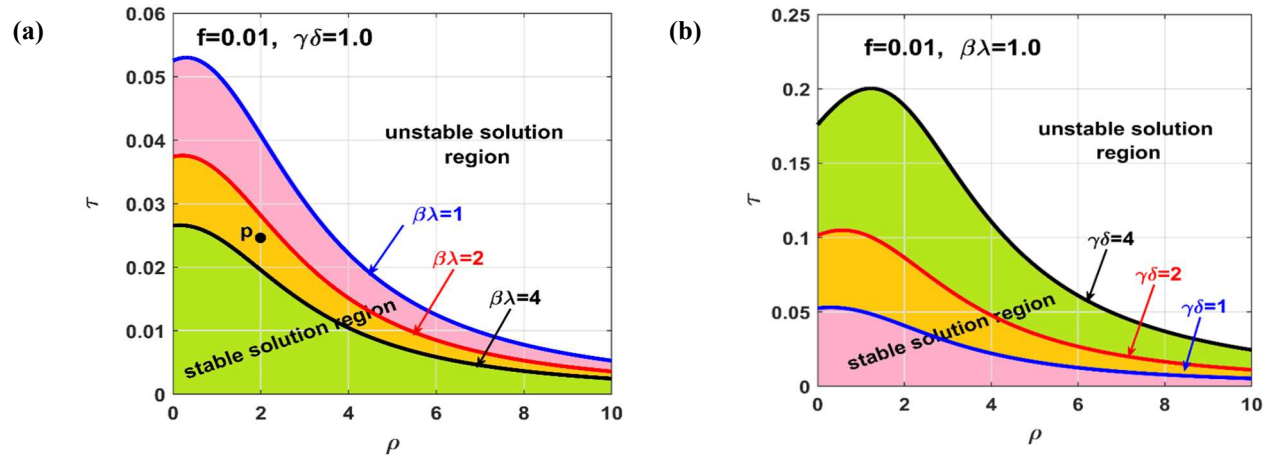

Figure 17. Stability margin of the loop-delay τ against ρ: (a) stability margin of τ against ρ at various values of $\beta\lambda$, and (b) stability margin of τ against ρ at various values of $\gamma\delta$.

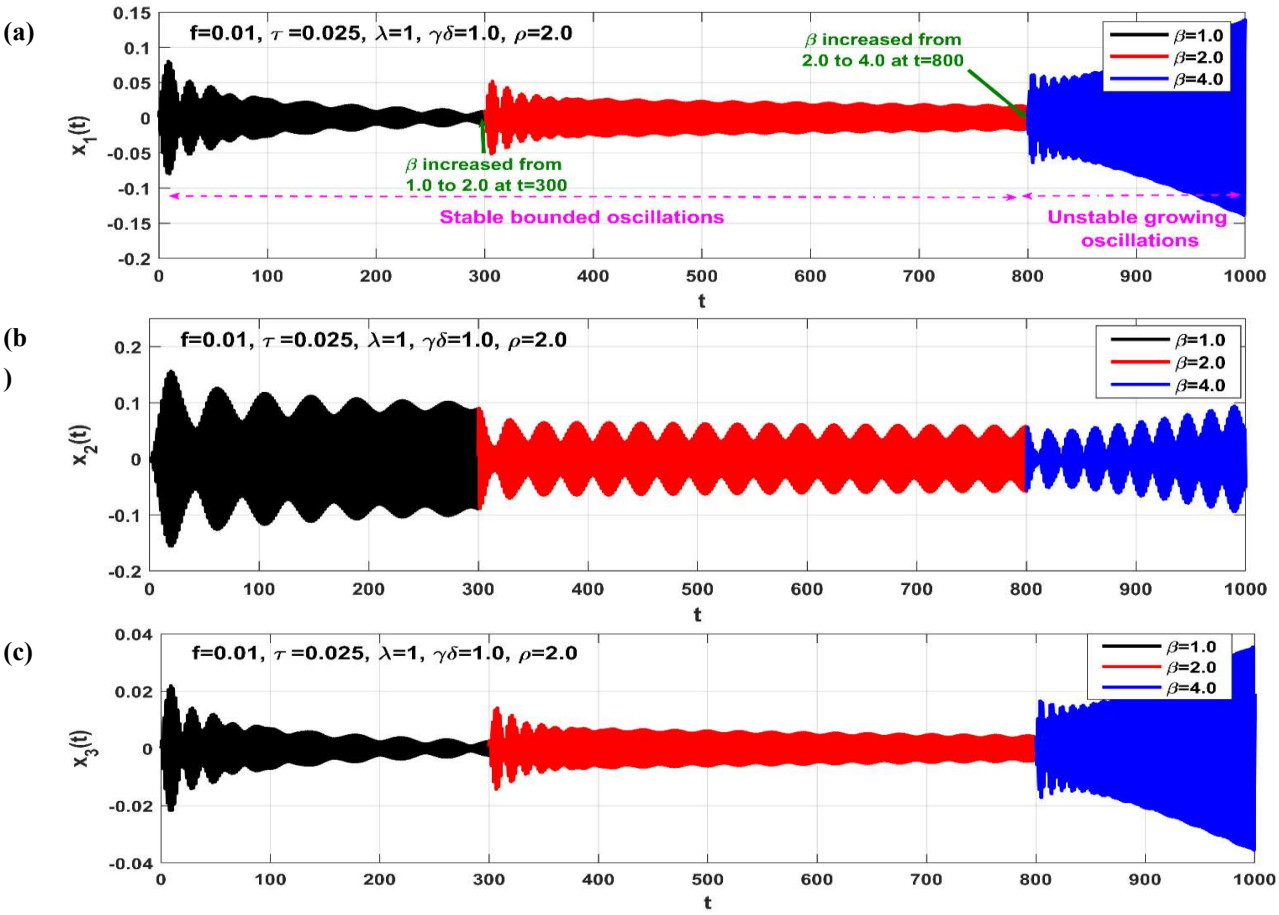

Figure 18. Controlled structure time-response corresponding to the marked point P (i.e., when $\tau = 0.025$ and $\rho = 2.0$) shown on the stability chart in Figure 17(a) when $\beta\lambda$ is increased from 1.0 to 2.0 at $t = 300$, and then further increased from 2.0 to 4.0 at $t = 800$.

The stability chart in the $\tau - \mu_1$ space is presented in Figure 19 for various values of the control keys $\beta\lambda$ and $\gamma\delta$. In Figure 19(a), τ is plotted against the structure damping coefficient μ_1 for $\gamma\delta = 1.0$ at three different $\beta\lambda$ values. Figure 19(b) shows τ plotted against μ_1 for three different $\gamma\delta$ values, with $\beta\lambda$ held constant at 1.0. Overall, Figure 19 illustrates that the loop-delay stability margin is a linearly decreasing function of the structure damping coefficient. This implies that higher μ_1 values will lead to system instability even with minimal delays in the closed-loop system. Additionally, although Figure 19(a) indicates that increasing the control key $\beta\lambda$ reduces the loop-delay stability margin, this reduction can be mitigated by increasing the first-order filter control gain $\gamma\delta$, as shown in Figure 19(b).

In Figure 20, the stability chart in the $\tau - \mu_2$ space is presented, highlighting the impact of the control gains $\beta\lambda$ and $\gamma\delta$. The chart reveals that the time-delay stability margin is nonlinearly proportional to the linear damping of the second-order filter, indicating that an increase in μ_2 can enhance the stability margin of the closed-loop system. This behavior contrasts with the effect of the structure-damping coefficient μ_1. Figure 20(a) shows that increasing the control key $\beta\lambda$ narrows the loop-delay stability margin, while Figure 20(b) illustrates that increasing $\gamma\delta$ broadens this margin. Despite the potential improvement in stability margin with a higher μ_2, it can compromise vibration suppression efficiency by interrupting the energy transfer that channel excessive vibration energy from the structure to the second-order filter. Therefore, μ_2 should be minimized (i.e., $\mu_2 \to 0^+$), while countering the destabilizing effects of τ by increasing $\gamma\delta$. Figure 21(a) plots the loop delay τ against the driving force amplitude f for $\beta\lambda$ values of 1.0, 2.0, and 4.0. Figure 21(b) displays the time delay stability margin in the $\tau - f$ space for $\gamma\delta$ values of $1.0, 2.0,$ and 4.0. Overall, Figure 21 demonstrates that there is no dependence between the loop-delay stability margin and the amplitude of the driving force that drives the structure.

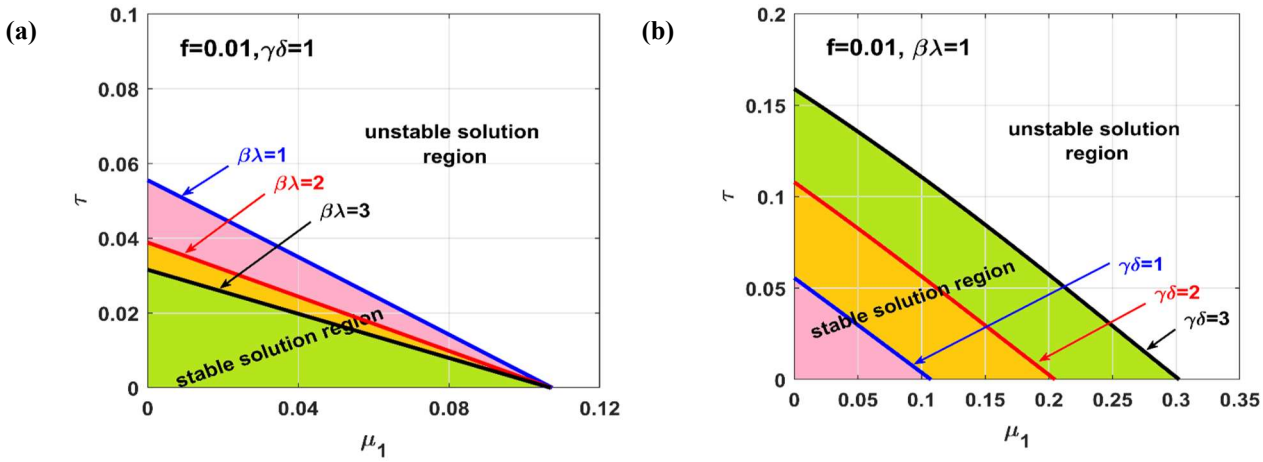

Figure 19. Stability margin of the loop-delay τ against the structure damping coefficient: (a) stability margin of τ against μ_1 when $\beta\lambda = 1.0, 2.0,$ and 4.0, (b) stability margin of τ against μ_1 when $\gamma\delta = 1.0, 2.0,$ and 4.0.

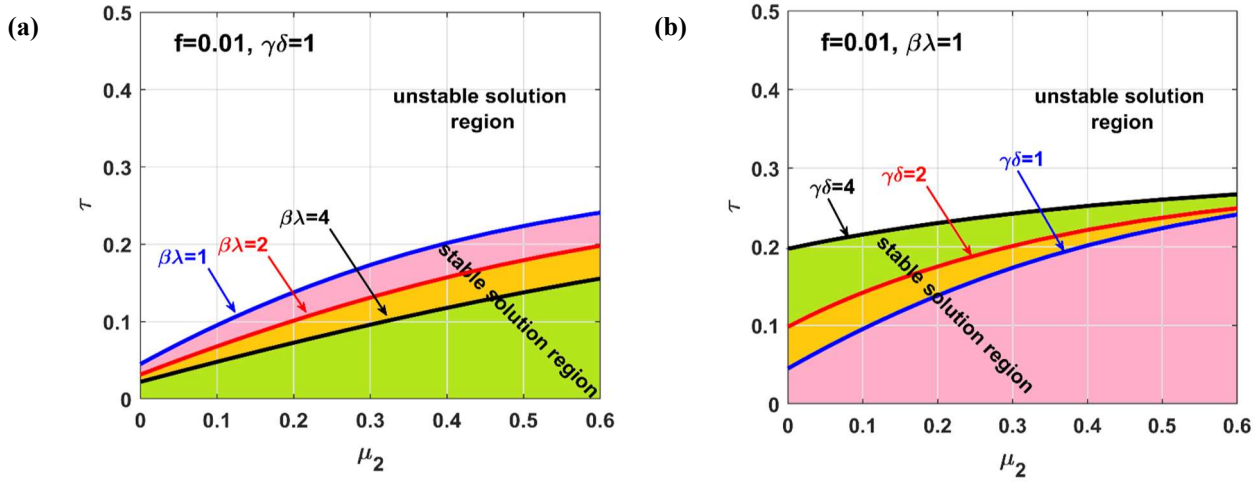

Figure 20. Stability margin of the loop-delay τ against the second-order filter damping coefficient: (a) stability margin of τ against μ_2 when $\beta\lambda = 1.0, 2.0,$ and 4.0, and (d) stability margin of τ against μ_2 when $\gamma\delta = 1.0,\ 2.0,$ and 4.0.

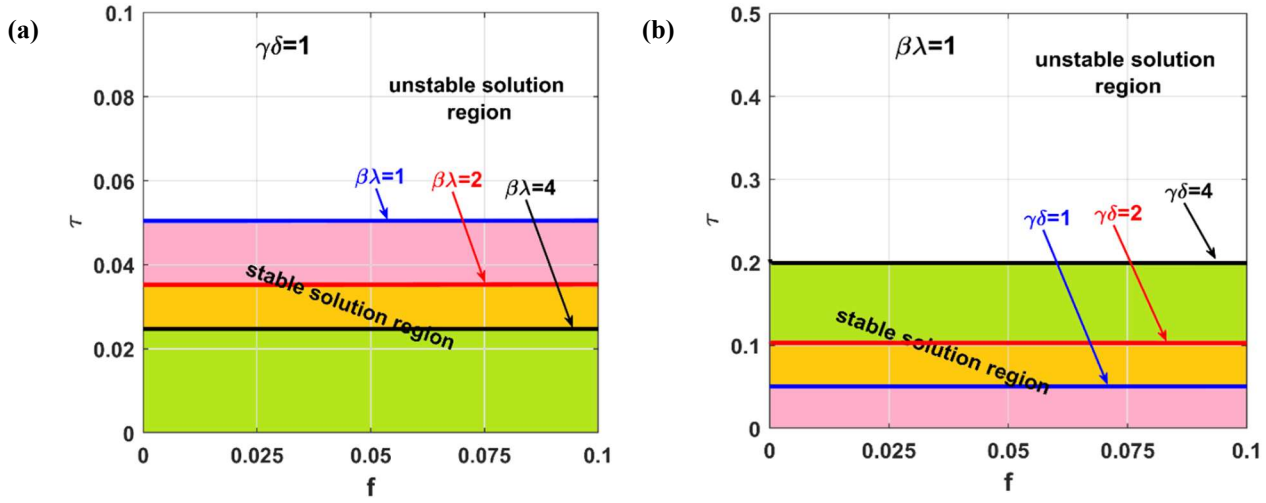

Figure 21. Stability margin of the loop-delay τ against the excitation amplitude f: (a) τ against f when $\beta\lambda = 1.0, 2.0,$ and 4.0, and (b) stability margin of τ against f when $\gamma\delta = 1.0,\ 2.0,$ and 4.0.

Finally, the time-delay stability margin against the driving frequency $\Omega = \omega_1 + \sigma_1$ is illustrated in Figure 22. Figure 22(a) depicts the stable critical limits of the loop delay over the interval $-1 \leq \sigma_1 \leq 1$ for control key $\beta\lambda$ values of $1.0, 2.0,$ and 4.0, with $\gamma\delta$ fixed at 1.0. Conversely, Figure 22(b) shows the critical values of the loop delay versus σ_1 at three different values of $\gamma\delta$ when $\beta\lambda = 1.0$. In general, Figure 22 suggests that the stability of the loop delay appears largely unaffected by the driving frequency except near resonant conditions. Furthermore, the figure demonstrates a common observation: $\gamma\delta$ widens the stability margin of the loop delay while increasing $\beta\lambda$ tends to

diminish the critical limit of the loop delay, beyond which the system transitions into instability.

Figure 22(b) (with $f = 0.01$ and $\beta\lambda = 1.0$) indicates that a delay $\tau = 0.04$ in the control loop ensures system stability along the σ_1 axis as long as $\gamma\delta \geq 1.0$. This implies that the closed-loop time-delayed nonlinear system described by Eqs (2) to (4) remains stable for delay $\tau = 0.04$when $\gamma\delta \geq 1.0$. To illustrate this, the system response curves (i.e., a_1 and a_2) are plotted against σ_1 using Eqs (43) to (46) for $\tau = 0.04$ and $\gamma\delta = 1.0, 2.0,$ and 3.0 in Figure 23. Additionally, the analytical results are validated numerically (i.e., small circles in Figure 23) by solving Eqs (2) to (4) using the DDE23 solver. The excellent agreement between the analytical and numerical results, as well as the strong correspondence between Figure 23 and the stability charts in Figure 22(b), is evident. Furthermore, Figure 22(b) indicates that a delay of $\tau = 0.12$ in the control loop causes the system to exhibit unstable oscillations along the σ_1 axis when $\gamma\delta = 1.0$ or 2.0. However, increasing $\gamma\delta$ to 4.0 restores system stability regardless of the driving frequency. To illustrate this, the system response curves are plotted for $\tau = 0.12$ when $\gamma\delta = 2.0$ and 4.0, as shown in Figure 24. The accurate correspondence with the stability chart in Figure 24(b) is clear, where the system and controller exhibit unstable oscillation amplitudes along the σ_1 axis at $\gamma\delta = 2.0$, while increasing $\gamma\delta$ to 4.0 restores stability to the time-delayed control system.

To simulate the transition of the time-delayed system from an unstable to a stable state by increasing the control key $\gamma\delta$ from 2.0 to 4.0, with $\tau = 0.12$, Eqs (2) to (4) were solved using the DDE23 solver. This corresponds to the scenario depicted in Figure 24 at $\sigma_1 = 0.0$, as illustrated in Figure 25. Initially, the system's oscillation was simulated with $\gamma\delta = 2.0$ over the time interval $0 \leq t < 200$, the control gain $\gamma\delta$ was increased from 2.0 to 4.0, and the simulation continued until $t = 500$. The figure shows that the system experienced growing unstable oscillations during the interval $0 \leq t < 200$. However, increasing $\gamma\delta$ from 2.0 to 4.0 at $t = 200$ stabilized the system, causing the oscillations to decay back close to zero.

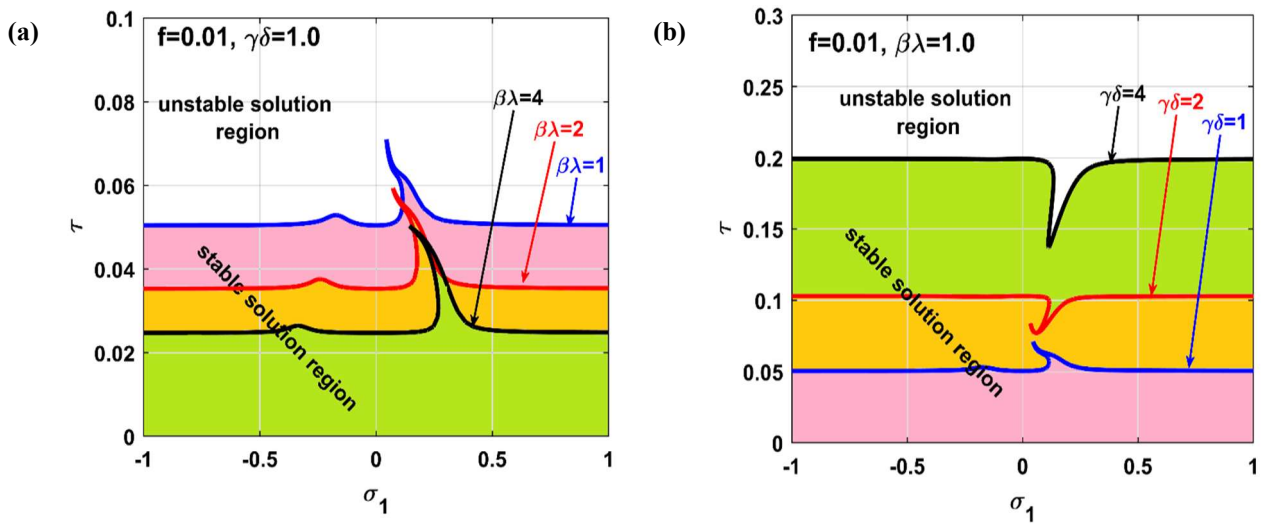

Figure 22. Stability margin of the loop-delay τ against the external excitation $\Omega = \omega_1 + \sigma_1$: (a) τ against σ_1 when $\beta\lambda = 1.0, 2.0,$ and 4.0, and (b) τ against σ_1 when $\gamma\delta = 1.0,\ 2.0,$ and 4.0.

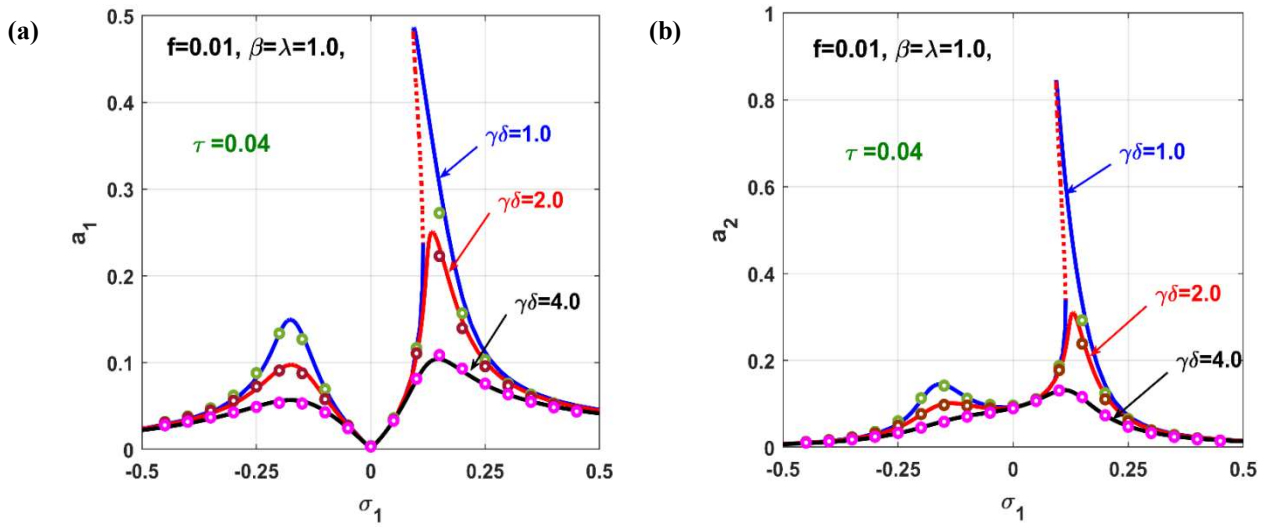

Figure 23. Response curves of the time-delayed system corresponding to Figure 22(b) when $\tau = 0.04$ (i.e., $f = 0.01, \beta\lambda = 1.0, \tau = 0.04$) at $\gamma\delta = 1.0, 2.0,$ and 4.0: (a) structure, and (b) second-order filter.

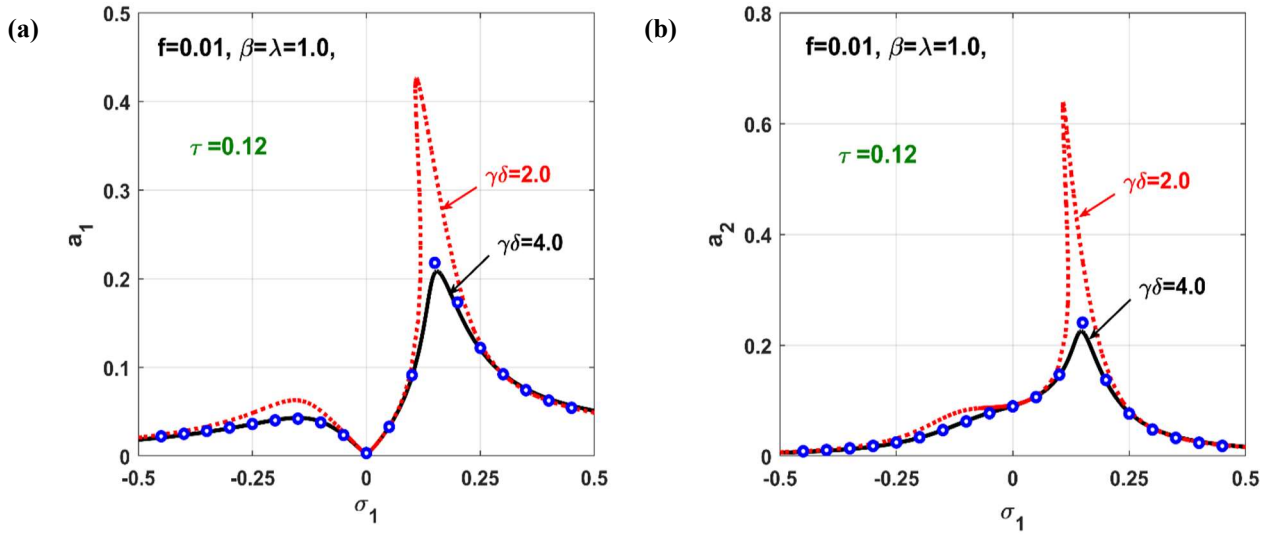

Figure 24. Response curves of the time-delayed control system corresponding to Figure 22(b) when $\tau = 0.12$ (i.e., $f = 0.01, \beta\lambda = 1.0, \tau = 0.12$) at $\gamma\delta = 2.0$ and 4.0: (a) structure, and (b) second-order filter.

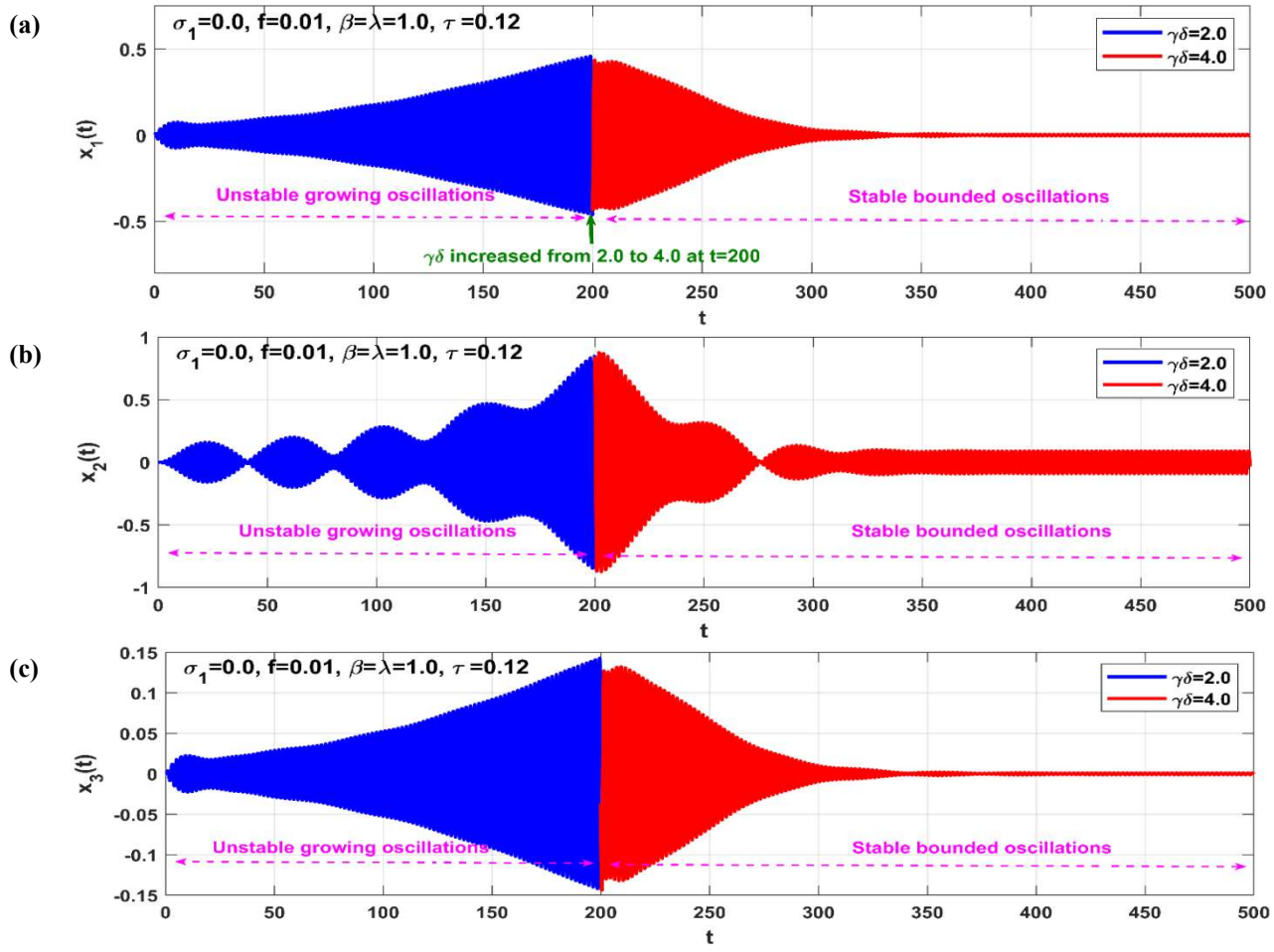

Figure 25. Controlled structure time-response corresponding to Figure 24 at $\sigma_1 = 0.0$ when $\gamma\delta$ is increased from 2.0 to 4.0 at the $t = 200$.

5. Conclusions

This work aims to stabilize unstable motion and eliminate resonant vibrations in a self-excited structure using an active control strategy, while thoroughly investigating the impact of time delay on control performance and system stability. The control strategy involves coupling the self-excited structure with both a second-order filter (with feedback gain λ, control gain β) and a first-order filter (with feedback gain δ, control gain γ). The dynamical model, incorporating time-delay τ, was developed and solved analytically, revealing a nonlinear algebraic system governing steady-state oscillation. Steady-state dynamics were analyzed using response curves and stability charts in terms of different control parameters and loop delay. Additionally, the full system response (transient and steady-state) was simulated numerically. Findings can be summarized as follows:

(1) The effectiveness of the second-order filter in eliminating oscillations of the self-excited structure hinges on the algebraic product of the control parameters β and λ, than their individual contributions. Notably, the amplitude of filter oscillations escalates with λ but diminishes with β, underscoring the need to minimize λ to prevent control signal saturation while prioritizing β as the primary control parameter.

(2) The equivalent damping of the closed-loop system correlates directly with the product of the control keys γ and δ, ensuring stabilization of negatively damped self-excited structures through effective utilization of the control key $\gamma\delta$.
(3) In general, the presence of a time delay in the control loop not only compromises the vibration suppression efficiency but also jeopardizes system stability when the delay surpasses a critical value called the time delay stability margin.
(4) The stability margin associated with time delay exhibits a nonlinear dependency on $\gamma\delta$, whereby increasing $\gamma\delta$ expands the stability margin of τ, ultimately increasing the control system's stability robustness against the loop delay.
(5) Conversely, the stability margin diminishes exponentially with increasing $\beta\lambda$, heightening the risk of system instability even with the minimal loop delay.
(6) The stability margin concerning loop delay diminishes linearly with the damping coefficient of the structure, signifying increased instability potential with higher μ_1 values even with the minimal delay in the control loop.
(7) The time-delay stability margin is nonlinearly proportional to the linear damping of the second-order filter, indicating that an increase in μ_2 can enhance the robustness of the control system against instability. Despite the potential improvement in stability margin with a higher μ_2, it can compromise vibration suppression efficiency by interrupting the energy transfer those channels excessive vibration energy from the structure to the filter. Therefore, μ_2 should be kept minimal (i.e., $\mu_2 \to 0^+$), while countering the destabilizing effects of τ by increasing $\gamma\delta$.
(8) Although the increase in the second-order filter gain $\beta\lambda$ narrows the loop stability margin, it can be concluded that loop delay does not pose a significant challenge in the proposed control method, as the adverse effects of increasing $\beta\lambda$ can be countered by increasing the control key $\gamma\delta$.
(9) Despite the loop-delay stability margin being inversely proportional to the damping coefficient of self-excited systems, which may cause system instability even with a small loop delay, especially for highly negatively damped structures, this drawback can be compensated by increasing the control key $\gamma\delta$ without affecting the established energy bridge between the structure and the second-order filter.

6. Evaluation against literature

In comparison with previously published studies on vibration control of self-excited structures, El-Badawy et al. [30], Jun et al. [31], and Warminski et al. [32] utilized a nonlinear saturation control method, which involved coupling a second-order filter nonlinearly to the target system. This technique was effective in mitigating resonant vibrations and stabilizing the system's unstable motion. Their results demonstrated that the control algorithm successfully reduced system vibrations when the controller's natural frequency was tuned to half of the system's excitation frequency. However, if these tuning conditions were not met, the closed-loop system risked losing stability, resulting in an amplification of vibration amplitudes instead of their suppression. Sarkar et al. [37] introduced a time-delayed positive position feedback controller to suppress the nonlinear vibrations of a self-excited structure under negligible external excitation. Using the describing function method, they investigated the closed-loop stability conditions, concluding that the presence of loop delay was detrimental, as it reduced the efficiency of vibration suppression. In [38], Saeed et al. coupled the self-excited structure with a first-order filter to evaluate the effectiveness of the integral resonant control technique in managing the nonlinear oscillations of the same system studied in [32,38]. They accounted for the impact of loop delay on the model and derived an objective function to optimize both control gains and loop delays for optimal

vibration suppression. The findings indicated that the integral resonant control method was robust against system instability caused by negative damping and loop delay. However, the main limitation of this controller, as well as those applied in [39,40], was the occurrence of high oscillations under resonant conditions, which was not observed with the control methods used in [30–32,37].

In this article, the control strategy involves simultaneously coupling the self-excited structure with both a second-order filter and a first-order filter, while incorporating loop delay into the model. The second-order filter functions as an energy bridge, channeling the structure's vibration energy away from the system. In contrast, the primary role of the first-order filter is to stabilize the closed-loop system. The main findings emphasize the controller's effectiveness in eliminating resonant vibrations and stabilizing non-resonant unstable motion. Moreover, by precisely adjusting the feedback and control gains of the two filters, the adverse effects of tuning loss or loop delay can be avoided, demonstrating superior efficiency compared to all techniques previously applied in the literature.

Author contributions

N. A. Saeed, L. Hou, and F. Z. Duraihem: Conceptualization; N. A. Saeed, A. Ashour, J. Awrejcewicz, and F. Z. Duraihem: Methodology; N. A. Saeed, L. Hou, and F. Z. Duraihem: Software; N. A. Saeed, A. Ashour, L. Hou, and J. Awrejcewicz: Validation; N. A. Saeed, A. Ashour, and L. Hou: Formal analysis; N. A. Saeed, A. Ashour, L. Hou, J. Awrejcewicz, and F. Z. Duraihem: Investigation; N. A. Saeed, and L. Hou: Writing-original draft preparation; N. A. Saeed, L. Hou, J. Awrejcewicz, and F. Z. Duraihem: Writing-review and editing; N. A. Saeed, A. Ashour, and F. Z. Duraihem: Visualization. All authors have read and agreed to the published version of the manuscript.

Acknowledgments

The authors are very grateful for the financial support from the National Key R&D Program of China (Grant No. 2023YFE0125900). The authors extend their appreciation to King Saud University for funding this work through Researchers Supporting Project number (RSPD2024R535), King Saud University, Riyadh, Saudi Arabia. Also, this work has been supported by the Polish National Science Centre, Poland under the grant OPUS 18 No. 2019/35/B/ST8/00980.

Conflict of interest

The authors declare no conflict of interest.

References

1. A. Abadi, *Nonlinear dynamics of self-excitation in autoparametric systems*, Ph.D. Thesis, University of Utrecht, 2003.
2. S. H. Strogatz, *Nonlinear dynamics and chaos*, CRC Press, Broken Sound Parkway, NW, Boca Raton, USA, 2018.
3. J. Warminski, Nonlinear dynamics of self-, parametric, and externally excited oscillator with time delay: van der Pol versus Rayleigh models, *Nonlinear Dynam.*, **99** (2020), 35–56. https://doi.org/10.1007/s11071-019-05076-5
4. A. Tondl, T. Ruijgrok, F. Verhulst, R. Nabergoj, *Autoparametric resonance in mechanical systems*, Cambridge University Press, New York, 2000.

5. S. S. Oueini, A. H. Nayfeh, Single-mode control of a cantilever beam under principal parametric excitation, *J. Sound Vib.*, **224** (1999), 33–47.
6. J. Li, R. Y. Shen, H. X. Hua, Cubic velocity feedback control of high-amplitude vibration of a nonlinear plant to a primary resonance excitation, *Shock Vib.*, **14** (2007), 235782. https://doi.org/10.1155/2007/235782
7. B. Pratiher, Vibration control of a transversely excited cantilever beam with tip mass, *Arch. Appl. Mech.*, **82** (2012), 31–42.
8. C. X. Liu, Y. Yan, W. Q. Wang, Primary and secondary resonance analyses of a cantilever beam carrying an intermediate lumped mass with time-delay feedback, *Nonlinear Dynam.*, **97** (2019), 1175–1195. https://doi.org/10.1007/s11071-019-05039-w
9. N. A. Saeed, G. M. Moatimid, F. M. F. Elsabaa, Y. Y. Ellabban, Time-delayed control to suppress a nonlinear system vibration utilizing the multiple scales homotopy approach, *Arch. Appl. Mech.*, **91** (2021), 1193–1215. https://doi.org/10.1007/s00419-020-01818-9.
10. J. X. Li, Y. Yan, W. Q. Wang, Secondary resonance of a cantilever beam with concentrated mass under time delay feedback control, *Appl. Math. Model.*, **135** (2024), 131–148. https://doi.org/10.1016/j.apm.2024.06.039
11. J. Peng, Y. N. Li, L. X. Li, S. Lenci, H. X. Sun, Time-delay feedback control of a suspended cable driven by subharmonic and superharmonic resonance, *Chaos Soliton. Fract.*, **181** (2024), 114646. https://doi.org/10.1016/j.chaos.2024.114646
12. N. A. Saeed, S. I. El-Bendary, M. Sayed, M. S. Mohamed, S. K. Elagan, On the oscillatory behaviours and rub-impact forces of a horizontally supported asymmetric rotor system under position-velocity feedback controller, *Lat. Am. J. Solids Stru.*, **18** (2021), e349. https://doi.org/10.1590/1679-78256410
13. N. A. Saeed, G. M. Moatimid, F. M. Elsabaa, Y. Y. Ellabban, M. A. El-Meligy, M. Sharaf, Time-delayed nonlinear feedback controllers to suppress the principal parameter excitation, *IEEE Access*, **8** (2020), 226151–226166. https://doi.org/10.1109/ACCESS.2020.3044998
14. I. M. Díaz, E. Pereira, P. Reynolds, Integral resonant control scheme for cancelling human-induced vibrations in light-weight pedestrian structures, *Struct. Control Hlth*., **19** (2012), 55–69. https://doi.org/10.1002/stc.423
15. A. Al-Mamun, E. Keikha, C. S. Bhatia, T. H. Lee, Integral resonant control for suppression of resonance in piezoelectric micro-actuator used in precision servomechanism, *Mechatronics*, **23** (2013), 1–9. https://doi.org/10.1016/j.mechatronics.2012.10.001
16. N. A. Saeed, S. M. El-Shourbagy, M. Kamel, K. R. Raslan, M. K. Aboudaif, Nonlinear dynamics and static bifurcations control of the 12-pole magnetic bearings system utilizing the integral resonant control strategy, *J. Low Freq. Noise V. A.*, **41** (2022), 1532–1560. https://doi.org/10.1177/14613484221104818
17. J. D. J. MacLean, S. A. Sumeet, A modified linear integral resonant controller for suppressing jump phenomenon and hysteresis in micro-cantilever beam structures, *J. Sound Vib.*, **480** (2022), 115365. https://doi.org/10.1016/j.jsv.2020.115365
18. N. A. Saeed, G. M. Moatimid, F. M. Elsabaa, Y. Y. Ellabban, S. K. Elagan, M. S. Mohamed, Time-delayed nonlinear integral resonant controller to eliminate the nonlinear oscillations of a parametrically excited system, *IEEE Access*, **9** (2021), 74836–74854. https://doi.org/10.1109/ACCESS.2021.3081397
19. N. A. Saeed, M. S. Mohamed, S. K. Elagan, J. Awrejcewicz, Integral resonant controller to suppress the nonlinear oscillations of a two-degree-of-freedom rotor active magnetic bearing system, *Processes*, **10** (2022), 271. https://doi.org/10.3390/pr10020271

20. N. A. Saeed, E. Mahrous, E. A. Nasr, J. Awrejcewicz, Nonlinear dynamics and motion bifurcations of the rotor active magnetic bearings system with a new control scheme and rub-impact force, *Symmetry*, **13** (2021), 1502. https://doi.org/10.3390/sym13081502
21. L. Jun, Positive position feedback control for high amplitude vibration of a flexible beam to a principal resonance excitation, *Shock Vib.*, **17** (2010), 286736. https://doi.org/10.3233/SAV-2010-0506
22. C. Shin, C. Hong, W. B. Jeong, Active vibration control of clamped beams using positive position feedback controllers with moment pair, *J. Mech. Sci. Technol.*, **26** (2012), 731–740. https://doi.org/10.1007/s12206-011-1233-y
23. M. Eissa, M. Kamel, N. A. Saeed, W. A. El-Ganaini, H. A. El-Gohary, Time-delayed positive-position and velocity feedback controller to suppress the lateral vibrations in nonlinear Jeffcott-rotor system, *Menoufia J. Elect. Eng. Res.*, **27** (2018), 261–278. https://doi.org/10.21608/mjeer.2018.64548
24. G. Zhao, A. Paknejad, G. Raze, A. Deraemaeker, G. Kerschen, C. Collette, Nonlinear positive position feedback control for mitigation of nonlinear vibrations, *Mech. Syst. Signal Pr.*, **132** (2019), 457–470. https://doi.org/10.1016/j.ymssp.2019.07.005
25. N. A. Saeed, E. M. Awwad, T. Abdelhamid, M. A. El-Meligy, M. Sharaf, Adaptive versus conventional positive position feedback controller to suppress a nonlinear system vibrations, *Symmetry*, **13** (2021), 255. https://doi.org/10.3390/sym13020255
26. S. M. Dhobale, S. Chatterjee, Efficacy of a class of resonant nonlinear controllers of fractional-order for adaptive vibration control—Analysis, simulations and experiments, *Control Eng. Pract.*, **143** (2024), 105788. https://doi.org/10.1016/j.conengprac.2023.105788
27. A. Nayfeh, D. Mook, L. Marshall, Non-linear coupling of pitch and roll modes in ship motion, *J. Hydronautics*, **7** (1973), 145–152. https://doi.org/10.2514/3.62949
28. P. F. Pai, B. Wen, A. S. Naser, M. J. Schulz, Structural vibration control using PZT patches and non-linear phenomena, *J. Sound Vib.*, **215** (1998), 273–296. https://doi.org/10.1006/jsvi.1998.1612
29. J. Li, H. X. Hua, R. Y. Shen, Saturation-based active absorber for a non-linear plant to a principal external excitation, *Mech. Syst. Signal Pr.*, **21** (2007), 1489–1498. https://doi.org/10.1016/j.ymssp.2006.03.001
30. A. A. El-Badawy, T. N. N. El-Deen, Quadratic nonlinear control of a self-excited oscillator, *J. Vib. Control*, **13** (2007), 403–414. https://doi.org/10.1177/1077546307076283
31. J. Li, X. B. Li, H. X. Hua, Active nonlinear saturation-based control for suppressing the free vibration of a self-excited plant, *Commun. Nonlinear Sci.*, **15** (2010), 1071–1079. https://doi.org/10.1016/j.cnsns.2009.05.028
32. J. Warminski, M. P. Cartmell, A. Mitura, M. Bochenski, Active vibration control of a nonlinear beam with self-and external excitations, *Shock Vib.*, **20** (2013), 792795. https://doi.org/10.3233/SAV-130821
33. F. Kenmogne, M. Ouagni, H. Simo, A. Kammogne, B. Bayiha, M. Wokwenmendam, et al., Effects of time delay on the dynamical behavior of nonlinear beam on elastic foundation under periodic loadings: Chaotic detection and it control, *Results Phys.*, **35** (2022), 105305.
34. F. Kenmogne, P. Noah, E. Dongmo, F. Ebanda, B. Bayiha, M. Ouagni, et al., Effects of time delay on the dynamics of nonlinear beam on elastic foundation under Harmonic moving load: Chaotic detection and its control, *J. Vib. Eng. Tech.*, **10** (2022), 2327–2346.
35. F. Kenmogne, M. Wokwenmendam, H. Simo, A. Adile, P. Noah, M. Barka, et al., Effects of damping on the dynamics of an electromechanical system consisting of mechanical network of discontinuous coupled system oscillators with irrational nonlinearities: Application to sand sieves, *Chaos Soliton. Fract.*, **156** (2022), 111805.

36. F. Kenmogne, S. Noubissie, G. Ndombou, E. Tebue, A. Sonna, D. Yemélé, Dynamics of two models of driven extended jerk oscillators: Chaotic pulse generations and application in engineering, *Chaos Soliton. Fract.*, **152** (2021), 111291.
37. A. Sarkar, J. Mondal, S. Chatterjee, Controlling self-excited vibration using positive position feedback with time-delay, *J. Braz. Soc. Mech. Sci. Eng.*, **42** (2020), 464. https://doi.org/10.1007/s40430-020-02544-7
38. N. A. Saeed, J. Awrejcewicz, M. A Alkashif, M. S. Mohamed, 2D and 3D visualization for the static bifurcations and nonlinear oscillations of a self-excited system with time-delayed controller, *Symmetry*, **14** (2022), 621. https://doi.org/10.3390/sym14030621
39. J. Mondal, S. Chatterjee, Controlling self-excited vibration of a nonlinear beam by nonlinear resonant velocity feedback with time-delay, *Int. J. Nonlin. Mech.*, **131** (2021), 103684. https://doi.org/10.1016/j.ijnonlinmec.2021.103684
40. A. Sarkar, J. Mondal, S. Chatterjee, Controlling self-excited vibration using acceleration feedback with time-delay, *Int. J. Dynam. Control*, **7** (2019), 1521–1531. https://doi.org/10.1007/s40435-019-00577-y
41. A. Nayfeh, Nonlinear interactions, analytical, computational and experimental methods, *Appl. Mech. Rev.*, 2000. https://doi.org/10.1115/1.1383674
42. A. Nayfeh, D. Mook, *Nonlinear oscillations*, Wiley, New York, 1979.
43. J. J. E. Slotine, W. Li, *Applied non-linear control*, Prentice Hall, Englewood Cliffs, 1991.
44. N. A. Saeed, M. S. Mohamed, S. K. Elagan, Periodic, quasi-periodic, and chaotic motions to diagnose a crack on a horizontally supported nonlinear rotor system, *Symmetry*, **12** (2020), 2059. https://doi.org/10.3390/sym12122059
45. K. H. Sun, X. Liu, C. X. Zhu, The 0-1 test algorithm for chaos and its applications, *Chin. Phys. B*, **19** (2010), 110510. Available from: https://iopscience.iop.org/article/10.1088/1674-1056/19/11/110510.
46. L. F. Shampine, S. Thompson, Solving DDEs in MATLAB, *Appl. Numer. Math.,* **37** (2001), 441–458.

Appendix

$$N_{11} = \frac{\mu_1}{2} - \frac{\gamma\delta}{2(\rho^2+\omega_1^2)}\cos(2\omega_1\tau) - \frac{\gamma\delta\rho}{2\omega_1(\rho^2+\omega_1^2)}\sin(2\omega_1\tau) - \frac{9}{8}\alpha_2\omega_1^2 h_1^2,$$

$$N_{12} = \frac{\beta}{2\omega_1}\sin(h_4 - \omega_2\tau),$$

$$N_{13} = \frac{\Omega^2 f}{2\omega_1}\cos(h_3),$$

$$N_{14} = \frac{\beta h_2}{2\omega_1}\cos(h_4 - \omega_2\tau),$$

$$N_{21} = \left(-\frac{3\alpha_1}{4\omega_1} + \frac{\alpha_3\omega_1^2}{2\omega_1}\right)h_1 - \frac{\beta h_2}{2\omega_1 h_1^2}\cos(h_4 - \omega_2\tau) - \frac{\Omega^2 f}{2\omega_1 h_1^2}\cos(h_3),$$

$$N_{22} = \frac{\beta}{2\omega_1 h_1}\cos(h_4 - \omega_2\tau),$$

$$N_{23} = -\frac{\Omega^2 f}{2\omega_1 h_1}\sin(h_3),$$

$$N_{24} = -\frac{\beta h_2}{2h_1\omega_1}\sin(h_4 - \omega_2\tau),$$

$$N_{31} = -\frac{\lambda}{2\omega_2}\sin(h_4 + \omega_1\tau),$$

$$N_{32} = -\frac{\mu_2}{2},$$

$$N_{33} = 0,$$

$$N_{34} = -\frac{\lambda h_1}{2\omega_2}\cos(h_4 + \omega_1\tau),$$

$$N_{41} = \left(-\frac{3\alpha_1}{4\omega_1} + \frac{\alpha_3\omega_1^2}{2\omega_1}\right)h_1 - \frac{\lambda}{2\omega_2 h_2}\cos(h_4 + \omega_1\tau) - \frac{\beta h_2}{2\omega_1 h_1^2}\cos(h_4 - \omega_2\tau) - \frac{\Omega^2 f}{2\omega_1 h_1^2}\cos(h_3),$$

$$N_{42} = \frac{\lambda a_1}{2\omega_2 h_2^2}\cos(h_4 + \omega_1\tau) + \frac{\beta}{2\omega_1 h_1}\cos(h_4 - \omega_2\tau),$$

$$N_{43} = \frac{\Omega^2 f}{2\omega_1 h_1}\sin(h_3),$$

$$N_{44} = \frac{\lambda h_1}{2\omega_2 h_2}\sin(h_4 + \omega_1\tau) - \frac{\beta h_2}{2\omega_1 h_1}\sin(h_4 - \omega_2\tau).$$